Modeling and Model Updating of a Full-Scale Experimental Base-Isolated Building

Tianhao Yu[a], Erik A. Johnson[a,*], Patrick T. Brewick[a,1], Richard E. Christenson[b], Eiji Sato[c], Tomohiro Sasaki[d]

[a]*Sonny Astani Department of Civil and Environmental Engineering, University of Southern California, Los Angeles, CA 90089, USA*
[b]*Department of Civil and Environmental Engineering, University of Connecticut, Storrs, CT 06269, USA*
[c]*Hyogo Earthquake Engineering Research Center, National Research Institute for Earth Science and Disaster Resilience, Hyogo 673-0515, Japan*
[d]*Structural Engineering Department, Technical Research Institute, Technology Division, Obayashi Corporation, Tokyo 204-8558, Japan*

Abstract

Large-scale seismic structural tests are crucial to validating both structural design methodologies and the effectiveness of seismic isolation devices. However, considering the significant costs of such tests, it is essential to leverage data from completed tests by taking advantage of numerical models of the tested structures, updated using data collected from the experiments, to complete additional studies that may be difficult, unsafe or impossible to physically test. However, updating complex numerical models poses its own challenges. The first contribution of this paper is to develop a multi-stage model

*Corresponding author at: Sonny Astani Department of Civil and Environmental Engineering, University of Southern California, Los Angeles, California 90089, USA.
Email address: JohnsonE@usc.edu (Erik A. Johnson)
[1]Present address: Department of Civil and Environmental Engineering and Earth Sciences, 156 Fitzpatrick Hall, Notre Dame, IN 46556, USA.

updating method suitable for high-order models of base-isolated structures, which is motivated and evaluated through modeling and model updating of a full-scale four-story base-isolated reinforced-concrete frame building that was tested in 2013 at the NIED E-Defense laboratory in Japan. In most studies involving model updating, all to-be-updated parameters are typically updated simultaneously; however, given the observation that the superstructure in this study predominantly moves as a rigid body in low-frequency modes and the isolation layer plays a minor role in all other modes, this study proposes updating parameters in stages: first, the linear superstructure parameters are updated so that its natural frequencies and mode shapes match those identified via a subspace system identification of the experimental building responses to low-level random excitations; then, the isolation-layer device linear parameters are updated so that the natural frequencies, damping ratios and mode shapes of the three isolation modes match. These two stages break a large-scale linear model updating problem into two smaller problems, thereby reducing the search space for the to-be-updated parameters, which generally reduces computational costs regardless of what optimization algorithm is adopted. Due to the limited instrumentation, the identified modes constitute only a subset of all the modes; to match each identified mode with a FEM mode, a procedure is proposed to compare each identified mode with a candidate set of FEM modes and to select the best match, which is a second contribution. Further, nonlinear isolation-layer device models are proposed, updated and validated with experimental data. Finally, combining

the isolation-layer devices' nonlinear models with the updated superstructure linear FEM, the final result is a data-calibrated nonlinear numerical model that will be used for further studies of controllable damping and validation of new design methodologies, and is being made available for use by the research community, alleviating the dearth of experimentally-calibrated numerical models of full-scale base-isolated buildings with lateral-torsional coupling effects.
Keywords: Base isolation, finite element model, model updating, system identification

1. Introduction

In many countries around the world, including the United States, earthquakes have caused severe damage to buildings and infrastructure and are one of the major concerns in the field of civil engineering. Many protective measures have been taken to minimize the seismic responses of structures; among these measures, base isolation has been widely adopted in recent decades (Constantinou et al., 1990; Mokha et al., 1993; Sato et al., 2013). Although the behaviors of base-isolated buildings have been extensively analyzed in previous research, full-scale seismic tests of these buildings are limited in quantity due to the high costs of such experiments (Brewick et al., 2018). However, such tests, like the series of tests investigated in this study, are vital to understanding the true performance of structures and for validating and innovating new base isolation techniques. Although some conclusions drawn

from the analysis of a particular base-isolated building may be unique to that building, other conclusions can deepen our knowledge of general base-isolated building behavior.

Given the high costs of full-size seismic tests, it is essential to leverage data from completed tests by utilizing a test structure's numerical models, that have been subsequently calibrated from the experimental data, to pursue additional studies that could not be tested in the laboratory or in the field. Such studies may include responses to additional earthquake records — including those too severe to safely test or even beyond laboratory capability — as well as damage detection technique validations, novel seismic control strategies, retrofit effects, and new design methodology verification. In these scenarios, finite element models (FEMs) of the experimental structure can be formulated and become powerful tools for researchers to evaluate the structural performance in subsequent studies. However, before ensuring that the model's key features (natural frequencies, mode shapes, energy dissipation pattern, *etc.*) are sufficiently close to those of the tested building, the trustworthiness of model results is indeterminate. Thus, however challenging it may be, model updating is a vital step between the experiments and subsequent model use in future studies.

Model updating methods may be characterized into four categories of methods: modal (Moaveni et al., 2009; Bakir et al., 2007, 2008; Friswell and Mottershead, 2013), frequency response function (FRF) (Lin and Ewins, 1994; Imregun et al., 1995; Lin and Zhu, 2006; Lin, 2011; Shadan et al.,

2016), modal strain energy (MSE) (Wang and Xu, 2019; Stubbs et al., 1995; Shi et al., 1998; Yang et al., 2020; Cornwell et al., 1999), and probabilistic (Bayesian) (Beck and Arnold, 1977; Beck and Katafygiotis, 1998a,b; Vanik et al., 2000; Beck et al., 2001; Jang and Smyth, 2017a). In modal methods, the model parameters are updated so that the FEM's modal properties (natural frequencies, damping ratios and mode shapes) match those of the experimental structure. FRF methods — proposed in Lin and Ewins (1994) for analytical models and in Imregun et al. (1995) for numerical models, and utilized in other studies (Lin and Zhu, 2006; Lin, 2011; Shadan et al., 2016) — update the model parameters so that the FEM transfer functions reproduce those computed from the experiment's input and output measurements; thus, modal property estimation, through system identification from the experimental data is not required (as it is for modal methods). MSE methods explore the differences in modal strain energy between the FEM and the experimental structure to update the model parameters; since proposed in 1995 (Stubbs et al., 1995), MSE methods have been successfully applied to model updating of beam structures (Yang et al., 2020) and plate structures (Cornwell et al., 1999), and a variant called the cross-MSE method (Hu et al., 2007, 2006; Wang et al., 2015) was successfully applied to three-dimensional truss structures. It is believed that the modal strain energy is more sensitive to model parameter changes, though it is also sensitive to noise, which limits its effectiveness in tests with noisy experimental data. Bayesian methods, the most common stochastic model updating methods, utilizes Bayes' inference

theorem to provide the probability distribution of (instead of just the best) model parameters, making it robust to uncertainties. For example, Ierimonti et al. (2020) used a continuous Bayesian model updating method to update the bilinear isolation-layer device models of a base-isolated RC building with the superstructure surrogate model constructed by the quadratic response surface method, achieving long-term monitoring of the isolation-layer devices.However, the significant computational cost to update the model of a complicated structure can be a challenge; for example, updating the 22 parameters of a bridge structure FEM, constructed with 19,632 beam elements and 1,464 truss elements, took three months to generate enough posterior samples (Jang and Smyth, 2017a). Although these applications of the aforementioned methods used linear model updating, some studies (*e.g.*, Song et al., 2009a,b, 2012) have also incorporated nonlinearities (*e.g.*, nonlinear material models), but are often applied only to laboratory-scale data.

In this study, several approaches are proposed for updating a partially nonlinear, high-order FEM of a base-isolated structure, motivated by and applied to updating a detailed model of a full-scale base-isolated structure using response data from the specimen's 2013 shake table tests at Japan's NIED "E-Defense" facility (Nakashima et al., 2018). The FEM involves approximately 85,000 degrees of freedom (DOFs); this level of model complexity effectively precludes capitalizing on Bayesian probabilistic methods because of computational cost. The MSE-based total least square cross-model cross-mode linear updating (Li et al., 2020) was attempted but resulted in a poor

match of the FEM and experimentally measured modal properties, likely due to MSE's sensitivity to the the sensor noise in this series of experiments. This leaves FRF and modal methods to consider.

One aspect that is particular to this structure is its base-isolated, not fixed-base, design that results in the superstructure moving approximately as a rigid body in the first three modes (isolation modes) and the deformations in all other modes (superstructure modes) mostly a result of superstructure behavior. For a base-isolated building like this, the superstructure model parameters can be updated first, and the isolation-layer parameters can be updated subsequently. As a direct result, one larger optimization problem is broken into two smaller problems (fewer modes to match and a smaller parameter space) that are easier and less time-consuming to solve (a previous study trying to update all parameters together took much longer and resulted in a sub-optimal match to the experimental results). Because modal methods treat each mode separately, and naturally separate the isolation modes from the superstructure modes, they are better choices than the FRF-based methods for the model updating of the base-isolated building in this study. Nevertheless, there are several challenges in applying two proposed stages of modal-based model updating method; these hurdles and the approaches proposed herein to address them are:

1. The rationale for separating the linear update into two stages is studied inYu (2022), which uses a simple 3DOF example with a stiffness distribution similar to that of the experimental building herein, and empiri-

cally demonstrates that: (a) isolation-layer linear stiffness changes have minor, and typically negligible, effects on the superstructure modes' natural frequencies and mode shapes; (b) superstructure linear stiffness changes have only marginal effect on the isolation modes' natural frequencies and mode shapes; and (c) superstructure damping changes have negligible influence on the isolation modes' damping ratios.

2. While the isolation modes are likely non-classically damped, due to the significant differences in stiffness and damping in the isolation layer relative to the superstructure, the superstructure modes are assumed to be proportionally damped. An analysis of the experimentally-identified mode shapes demonstrates that this assumption is reasonable.
3. Successful modal-based model updating reduces the error between each experimentally-identified mode and its corresponding FEM mode, which is often not the same mode number (when modes are sorted by increasing frequency) because: the unupdated FEM model's modes may be in a different order due to uncalibrated model parameters; identification from a limited sensor set may not be able to detect some modes; and measurement noise can result in spurious non-physical "identified" modes. While previous studies have successfully matched experimental and model modes for relatively simple structures based on frequency differences, different definitions of modal assurance criteria (Allemang and Brown, 1982; Lieven and Ewins, 1988), mass matrix compatibilities (Avitabile and O'Callahan, 1988; O'Callahan, 1995), comparisons of

modal energies (Bugeat and Lallement, 1976) and comparison of FRFs (Ibrahim, 1993), or for ones in which the mode matching is straightforward (*e.g.*, Jang and Smyth, 2017b), this specimen's limited sensor coverage and the high-order FEM poses a significant mode-matching challenge. To address this difficulty, a new efficient and effective mode-matching procedure is proposed.

4. Modal approaches are inherently based on linear system characteristics, but this structure's isolation layer is highly nonlinear, as is typical of most isolated buildings; thus, it must be determined whether superstructure nonlinearity is a factor. Herein, it is demonstrated for this structure that the identified natural frequencies of the corresponding superstructure modes, based on the random and the earthquake excitation test data, are nearly identical, which is consistent with base-isolation design intent for superstructure deformation; thus, this superstructure's nonlinearity is negligible during significant earthquake excitation, even with peak horizontal accelerations as much as $0.5g$. Finally, to simulate the building's nonlinear responses, the calibrated superstructure model is combined with isolation-layer device models — some bi-directional hysteretic parameter-calibrated (Brewick et al., 2020) Bouc-Wen models (Park et al., 1986; Wen, 1980) and some bi-linear stiffness models. The result is a locally nonlinear FEM that can faithfully reproduce the building's responses to earthquake ground motions.

In summary, the model updating is conducted through the following steps. (a) Perform system identification using experimental input-output (accelerometer) measurements to estimate the modal properties of the building. (b) Update the superstructure linear stiffnesses so that the natural frequencies and mode shapes of the FEM superstructure modes match those identified. (c) Update the linear stiffnesses and damping coefficients of the isolation-layer devices so that the natural frequencies, mode shapes and damping ratios of the FEM isolation modes match those identified. (d) Perform time-history analyses and compare the simulated responses with the experimental data to evaluate and demonstrate the success of model updating. (e) Calibrate nonlinear models of the isolation-layer devices, combine them with the superstructure model, and evaluate the resulting partially nonlinear FEM through its time-history responses to demonstrate model calibration success.

The remainder of this paper is organized as follows. Section 2 provides a brief review of the experiments with a focus on the experimental set-up used in this study. Section 3 summarizes the relevant system identifications that were partially reported in Brewick et al. (2018) as well as those new in this study. Sections 4–6 detail the linear model updating, including an introduction to the FEM, the formulation of the optimization algorithm, a summary of the updated FEM and a time-history analysis using the updated model. Section 7 focuses on the construction of the partially nonlinear FEM, including the isolation-layer devices' modeling and comparisons of the model-

predicted and measured earthquake responses, followed by the conclusions and the future work in Section 8.

2. Experimental Set-up

A 686-ton full-scale four-story base-isolated reinforced-concrete frame building (Figure 1) was tested in 2013 (Sato et al., 2013) on Japan's NIED (National Research Institute for Earth Science and Disaster Resilience) 6DOF shake table at the Hyogo Earthquake Engineering Research Center, best known as "E-Defense" (Ogawa et al., 2001). The geometric asymmetry and the corner stairway-core walls create significant lateral-torsional coupling in the superstructure responses. For the 8 August 2013 experiments concerned in this study, the isolation layer consisted of two rubber bearings (RBs), two elastic sliding bearings (ESBs) and two passive U-shaped steel yielding damper pairs (SDPs) (Figures 3 and 4). A series of experiments were con-

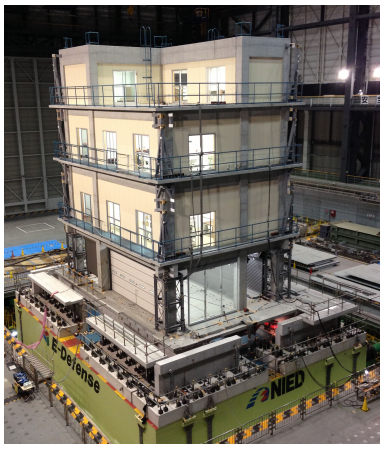

Figure 1: Experimental specimen (photo E.A. Johnson)

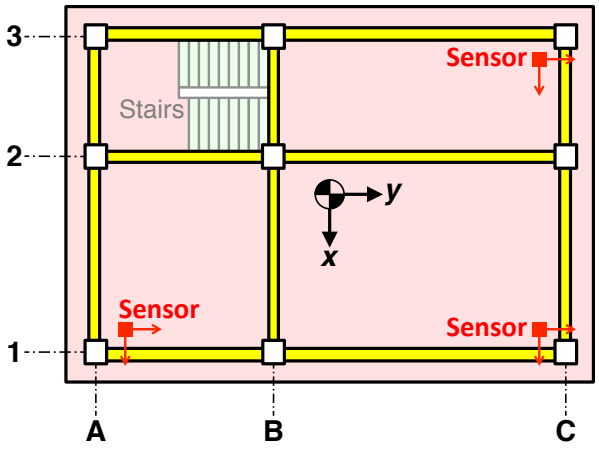

Figure 2: Accelerometer configuration on floors 0–3

ducted in August 2013 with excitations including low-intensity filtered white noise as well as scaled versions of both historical and synthetic earthquake records.

Various types of sensors — including displacement sensors, accelerometers and force transducers — were mounted on the superstructure and the shake table to monitor the time-history responses of the entire system. Specifically,

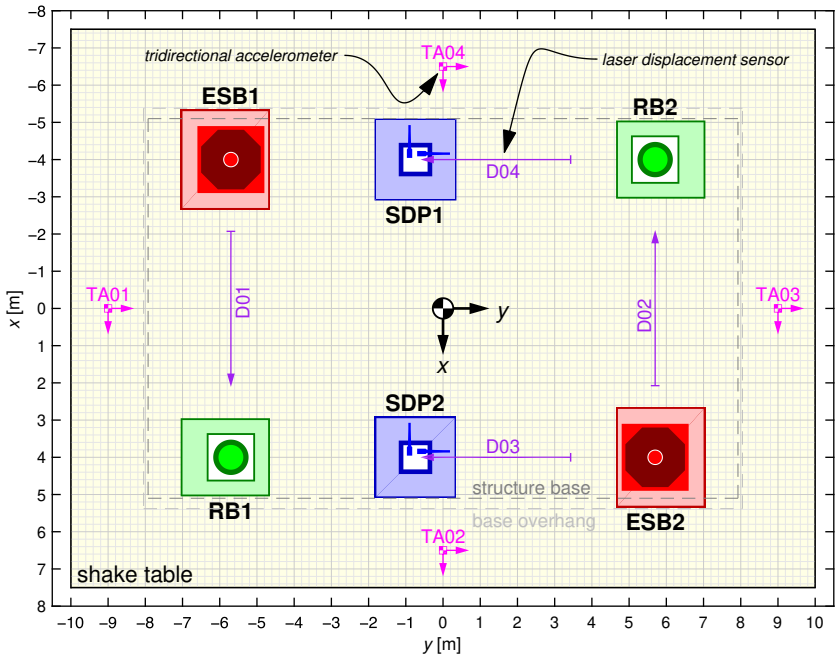

Figure 3: Isolation-layer layout

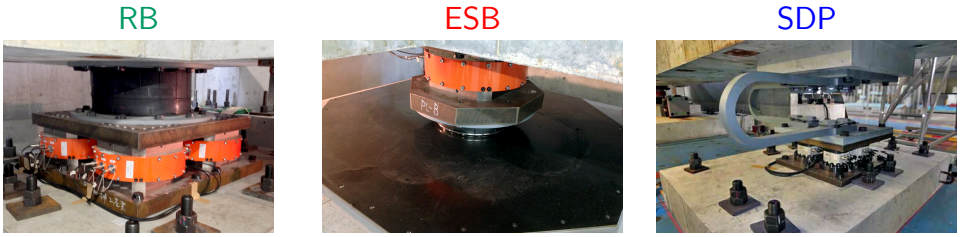

Figure 4: Isolation-layer devices (photos E.A. Johnson & T. Sasaki)

tri-directional accelerometers were placed at three corners on floors 0–3 (Figure 2) — where floor 0 is the superstructure base — and at two corners on the roof (floor 4), for a total of 14 locations and 42 (14×3) superstructure acceleration channels (x, y and z directions). Further, the shake table was instrumented with four tri-directional accelerometers, for a total of 12 (4×3) shake table acceleration channels, from which the 6×1 table-center acceleration vector $\ddot{\mathbf{x}}_{\mathrm{g}}(t)$ — composed of three translational and three rotational accelerations — is computed in a least squares sense, assuming that the table is rigid, using a transformation matrix determined from the sensor location geometry (Brewick et al., 2018). Force transducers were mounted under each isolation-layer device to measure the restoring forces. Unless otherwise noted, all signals were collected at a 1 kHz sampling rate and then low-pass filtered with a 35 Hz cutoff frequency (below the 60 Hz electrical frequency used at the testing facility).

This study focuses on the series of tests conducted on 8 August 2013 — including Tests 010–012 (different realizations of a random excitation) and Tests 013–016 (scaled versions of the March 2011 Mw9.0 Tohoku-Oki earthquake record from the KNET Furukawa station). Figure 5 shows the horizontal table-center accelerations in random excitation Test 010 and earthquake excitation Test 016 (the most intensive, as ranked by root-mean-square ground acceleration, of the Tohoku-Oki earthquake tests). The excitation records' peak accelerations and durations are provided in Table 1.

When subjected to the random excitation, both the superstructure and

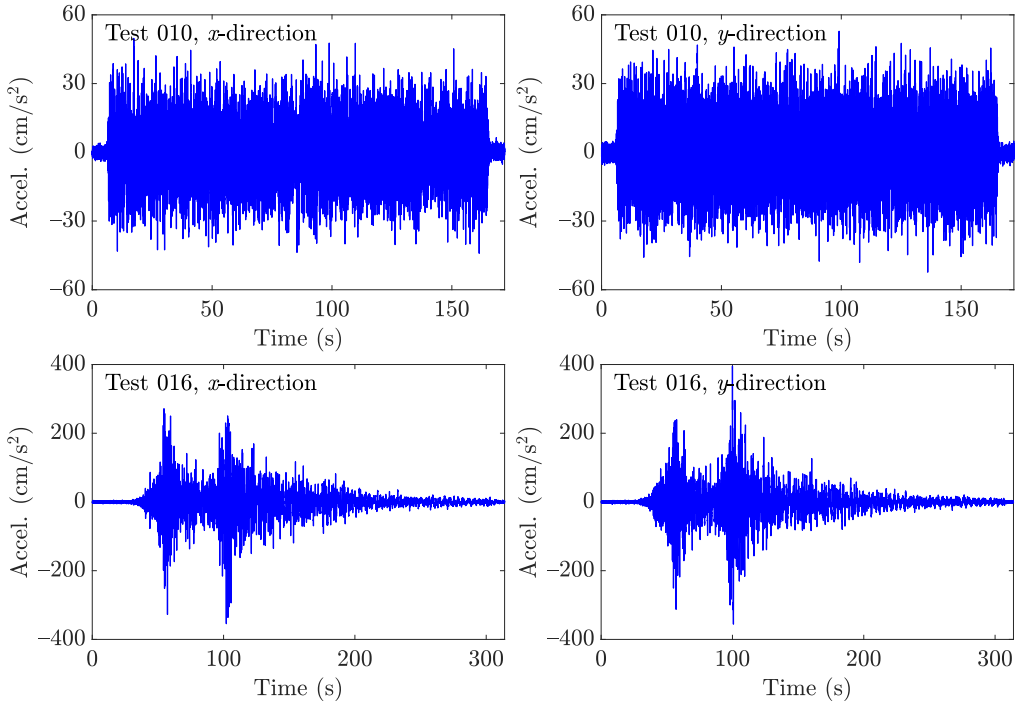

Figure 5: Shake table center accelerations, in the x and y directions, in Test 010 (random) and Test 016 (scaled March 2011 Tohoku-Oki earthquake)

Table 1: Descriptions of excitations

		Peak Acceleration (cm/s²)			
Test No.	**Excitation**	x	y	z	**Duration (s)**
010	6DOF Random	52.08	57.98	68.41	172.06
013	Tohoku-Oki EQ	243.89	300.32	170.10	314.90
014		415.81	432.98	363.74	314.91
015		347.66	480.95	224.81	314.93
016		356.21	398.14	222.99	314.95

the isolation-layer devices remain linear so that the isolation-layer devices can be reasonably modeled with a linear stiffness and a constant damping coefficient in each horizontal direction. The earthquake excitations, however,

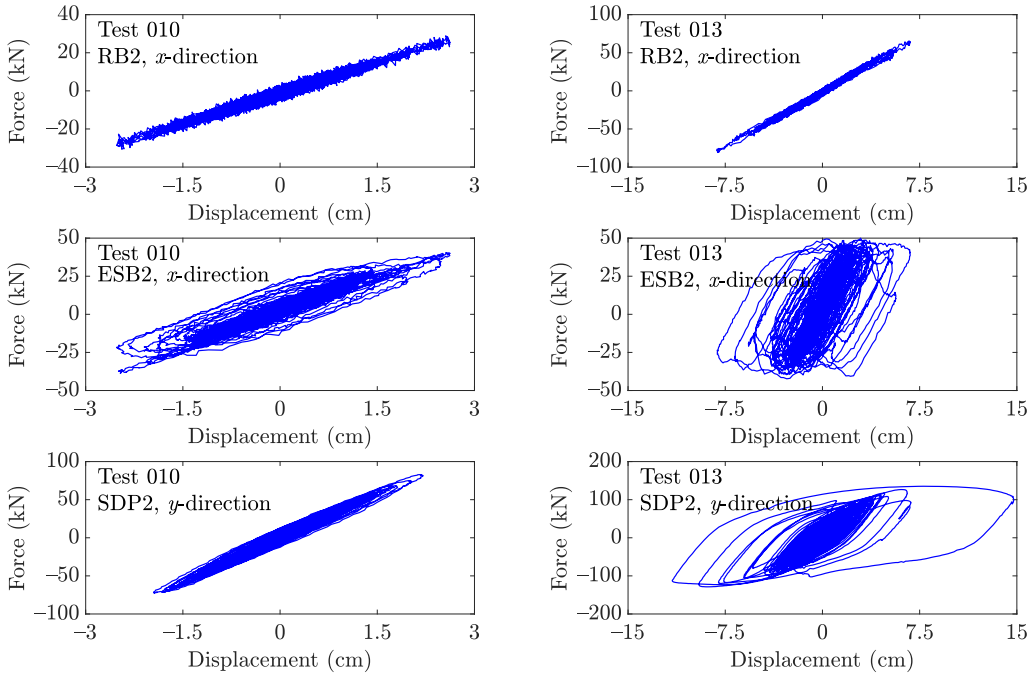

Figure 6: Representative linear and nonlinear force-displacement relationships in Tests 010 and 013, respectively (note that the scales differ)

as discussed in Section 3.2, induce mild nonlinearity in the rubber bearings and strong nonlinearity in the elastic sliding bearings and the U-shaped steel damper pairs (Figure 6), though the superstructure remains essentially linear.

3. System Identification

To estimate the modal properties from the experimental data — so that the FEM can be updated in Section 5 to match those properties — identification is performed based on the experimental data from Test 010, in which the building was subjected to low-level random excitations in all six shake table DOFs and remained primarily linear in both superstructure and isolation layer. Further, given that calibrated energy dissipation is crucial for

reproducing time-history responses and that the damping ratios in low-level motion might be different from the effective damping in large earthquake response, system identification is also performed based on data from Test 013, in which the input is a scaled March 2011 Tohoku-Oki earthquake record (Table 1), to determine effective natural frequencies and effective damping ratios.

3.1. Test 010

The primarily linear responses to the low-level random excitations were used, in a previous study (Brewick et al., 2018), to estimate modal properties (natural frequencies, damping ratios and mode shapes) through the N4SID (Subspace State Space System Identification) system identification method (Van Overschee and De Moor, 1994), which is a data-driven system identification method for combined deterministic-stochastic inputs. The 12 table acceleration responses were used as inputs to the building model and the 42 base and superstructure acceleration responses were the outputs. The table and structure accelerations were detrended, additionally low-pass filtered at 28.6 Hz (8th-order Chebyshev Type I filtered, first forward and then backward) and downsampled from 1 kHz to 71.4 Hz. When implementing the N4SID method, selecting the order of the model is always a challenge: too low and some physically important modes may fail to be identified; too high and spurious or redundant modes may also be "identified." Thus, the stabilization diagram strategy (Peeters, 2000) was used to choose the order and identify "stable" modes, which are defined to be modes identified at the optimal

model order that remain, at the next higher model order, within 1% frequency deviation and 5% damping ratio deviation, and have modal assurance criterion (MAC) values larger than 0.95 (stabilization diagrams for Test 010 are shown in Brewick et al., 2018). The $\mathrm{MAC}(\boldsymbol{\phi}_i, \boldsymbol{\phi}_j) = |\boldsymbol{\phi}_i^{\mathrm{H}} \boldsymbol{\phi}_j| / (\boldsymbol{\phi}_i^{\mathrm{H}} \boldsymbol{\phi}_i \boldsymbol{\phi}_j^{\mathrm{H}} \boldsymbol{\phi}_j)^{1/2}$ (superscript H denotes conjugate transpose) ranges from 0 to 1, where 0 indicates no similarity (orthogonal vectors) and 1 indicates a perfect match (parallel vectors) (Peeters, 2000; Vacher et al., 2010).

Table 2: Identified natural frequencies and damping ratios (Test 010) (adapted from Brewick et al., 2018)

	Mode	Frequency [Hz]	Damping Ratio [%]
Isolation	1	**0.6853**	**7.63**
	2	**0.6975**	**8.62**
	3	**0.7095**	**7.92**
Superstructure	4	**4.7812**	**3.21**
	5	**5.1749**	**3.41**
		6.1199	76.13
	6	**7.2931**	**3.17**
		10.0301	86.06
	7	**10.8364**	**3.50**
		11.5684	13.19
		14.5622	63.46
	8	**15.3463**	**3.26**

bold indicates fully stable identified mode

Table 3: Identified effective natural frequencies and damping ratios (Test 013)

	Mode	Frequency [Hz]	Damping Ratio [%]
Isolation	1	**0.6079**	**19.95**
	2	**0.6182**	**16.65**
	3	**0.7682**	**25.68**
Superstructure	4	**4.6415**	**4.60**
	5	**5.0268**	**3.59**
		5.4095	98.95
	6	**7.1137**	**3.40**
		7.4211	98.99
		7.7266	68.17
		8.3521	81.80
		9.0055	91.56
		9.5116	57.01
	7	**10.6261**	**4.14**
		11.3949	32.37
	8	**11.4646**	**4.57**
		13.6537	41.00
		14.5471	29.69
	9	**14.9861**	**3.54**

bold indicates fully stable identified mode

The identified frequencies and damping ratios with model order 66 are shown in Table 2. The first three modes have comparatively lower natural frequencies as intended, and are labeled "isolation modes." The remaining modes are labeled "superstructure modes." Because there are 42 output channels, each identified mode shape is a vector with 42 complex-valued entries; Figure 7 shows the directions of the mode shape's elements in the complex plane for each of the first eight identified modes. The mode shapes for identified modes 4–6, which move primarily in the horizontal directions, all have approximately one dominant direction, indicating that they are near-monophase and can be well approximated by their real parts; modes 7–8, which move primarily vertically, are less monophase but still much more so than isolation modes 1–3 — also indicated by the collinearity values (Juang and Pappa, 1985) shown in the figure. Thus, it is fair to assume that the superstructure modes are proportionally damped; as a result, the damping matrix need not be incorporated when updating the superstructure FEM to achieve a mode shape match. On the contrary, matching the nonclassically damped isolation modes must update the damping and stiffness simultaneously to achieve a mode shape match. This finding can also be demonstrated by evaluating the MAC values of the identified mode shapes against themselves (each mode has two complex-valued mode shapes that are complex conjugates of each other), as shown in Figure 8 (a larger square indicates a larger MAC value and a better match of two mode shapes). When a mode shape is near-monophase (modes 4–8), its conjugate is close to the original

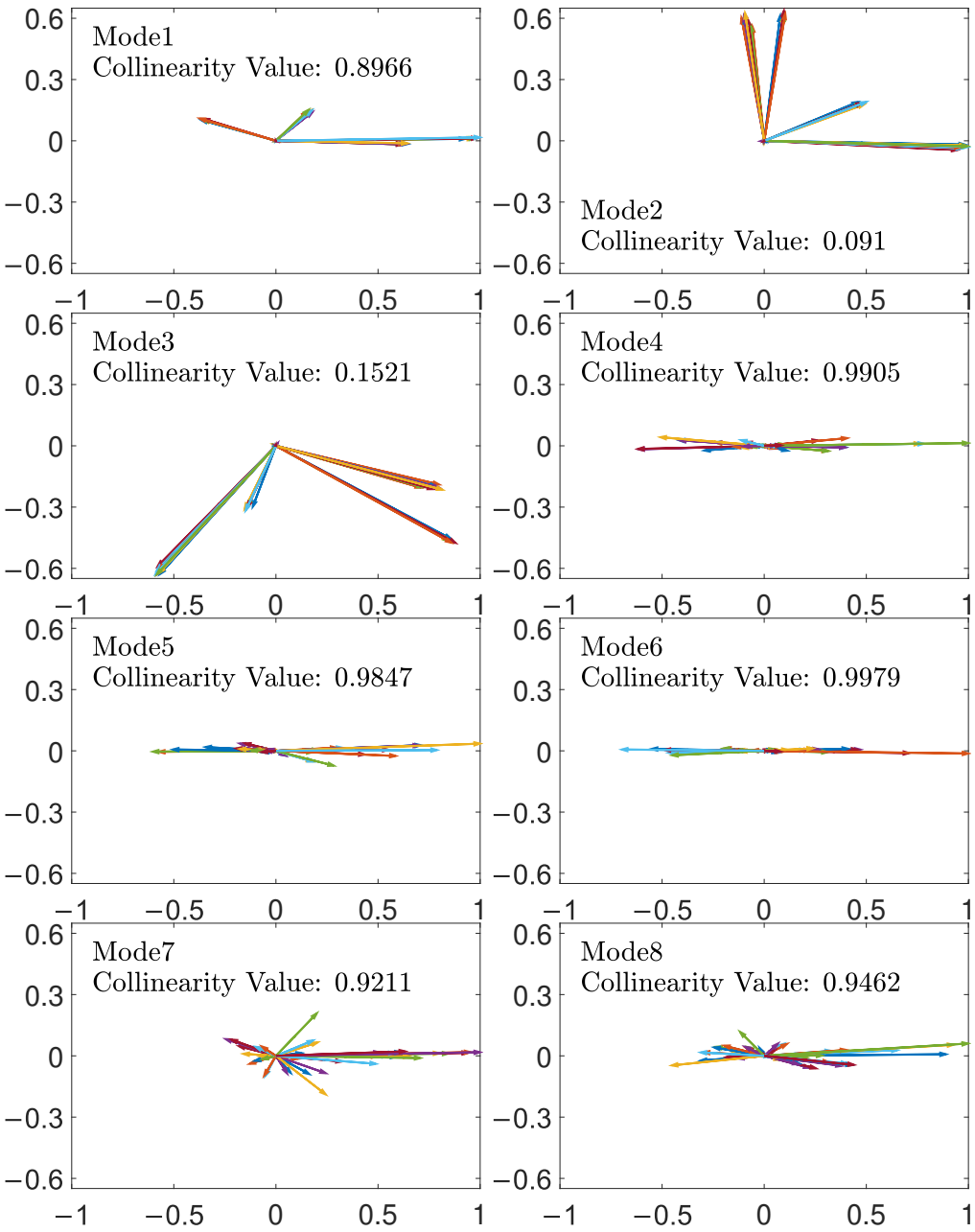

Figure 7: Identified mode shape vector elements in the complex plane

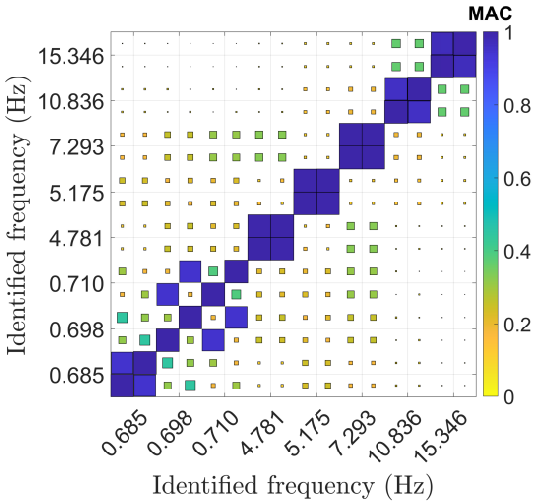

Figure 8: MAC values of the identified mode shapes against themselves (each natural frequency corresponds to two mode shapes that are complex conjugates of each other)

mode shape, and their MAC value will be near unity; this is not the case for nonmonophase mode shapes (modes 2–3).

3.2. Test 013

A similar methodology for system identification is applied to the experimental data from Test 013; this earthquake excitation, unlike the bandlimited white noise in Test 010, is quite non-Gaussian, though this is no difficulty for the N4SID identification since the shake table accelerations are the known input to the method. In this case, the input (table) and output (structure) accelerations were additionally low-pass filtered with a 30 Hz low-pass filter (FIR filter with no more than 0.1 dB variation below 30 Hz, and at least two orders of magnitude reduction above 35 Hz) and then downsampled (from 1 kHz to $333.\overline{3}$ Hz). With model order set to 66, the identified effective frequencies and damping ratios are shown in Table 3. Comparing Tables 2 and 3,

the natural frequencies of identified modes 4–8 do not change much, indicating at most a very mild nonlinearity in the superstructure during Test 013; indeed, most of the small changes are likely due to the strongly nonlinear isolation-layer devices.

4. Introduction to the Finite Element Model

The nominal FEM, shown in Figure 9, was developed based on the structural design drawings. The beams, columns, and shear walls were modeled by solid concrete elements and embedded reinforcing steel bars were modeled with truss elements; the floor slabs and the nonstructural walls (autoclaved lightweight concrete [ALC] panels) were modeled with shell elements; and the isolation-layer devices were modeled with spring elements. Approximations typically must be made when constructing FEMs, either because some details have little influence on the behavior of the building or because of

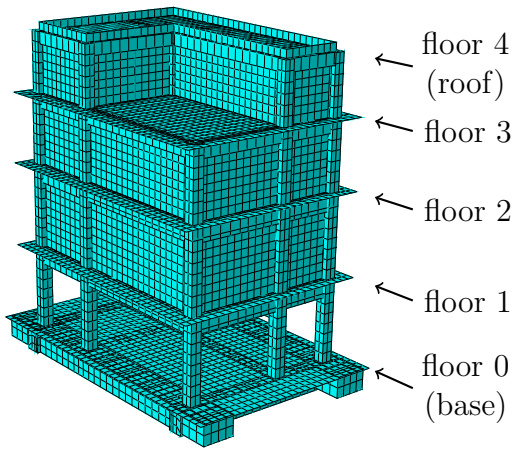

Figure 9: Finite element model

the vast effort required to include every minute detail; for example, it is assumed here that each structural member is internally homogenous (constant density, Young's modulus, *etc.*), floor slab loading from nonstructural components are ignored, and each nonstructural wall with window(s) is modeled as one homogeneous shell element.

To conveniently update the FEM, the global mass matrix $\mathbf{M}$, the nominal global stiffness matrix $\mathbf{K}_0$, and the global element stiffness matrices $\mathbf{K}_i$ induced by unit changes to the i^{th} to-be-updated parameter θ_i, $i = 1$, ..., n_θ, are extracted for the model updating analysis. Then, the stiffness matrix $\mathbf{K}$ given a specific parameter vector $\boldsymbol{\theta}$ can be written as $\mathbf{K} = \mathbf{K}_0 + \sum_{i=1}^{n_\theta} \mathbf{K}_i(\theta_i - \theta_i^{\text{nominal}})$, where $\boldsymbol{\theta}^{\text{nominal}}$ is the vector of nominal initial parameter values that correspond to nominal initial stiffness $\mathbf{K}_0$. The first six mode shapes of this nominal FEM are shown in Figure 10.

A preliminary study explored three choices for the set of FEM parameters to be updated.

- In Case I, the to-be-updated parameters $\boldsymbol{\theta}$ included the Young's moduli of the x- and y-direction beams under floors 0–4 (10 parameters), the columns in each story (4 parameters), the shear walls in each story (4 parameters), the floor slabs on each floor (5 parameters), the stairs in each story 1–3 (3 parameters; the stairs end at floor 3), and the stiffnesses and damping coefficients of the isolation-layer devices in both x and y directions (24 parameters; note that the low-level motion used to determine the modal parameters for the linear updating induces small

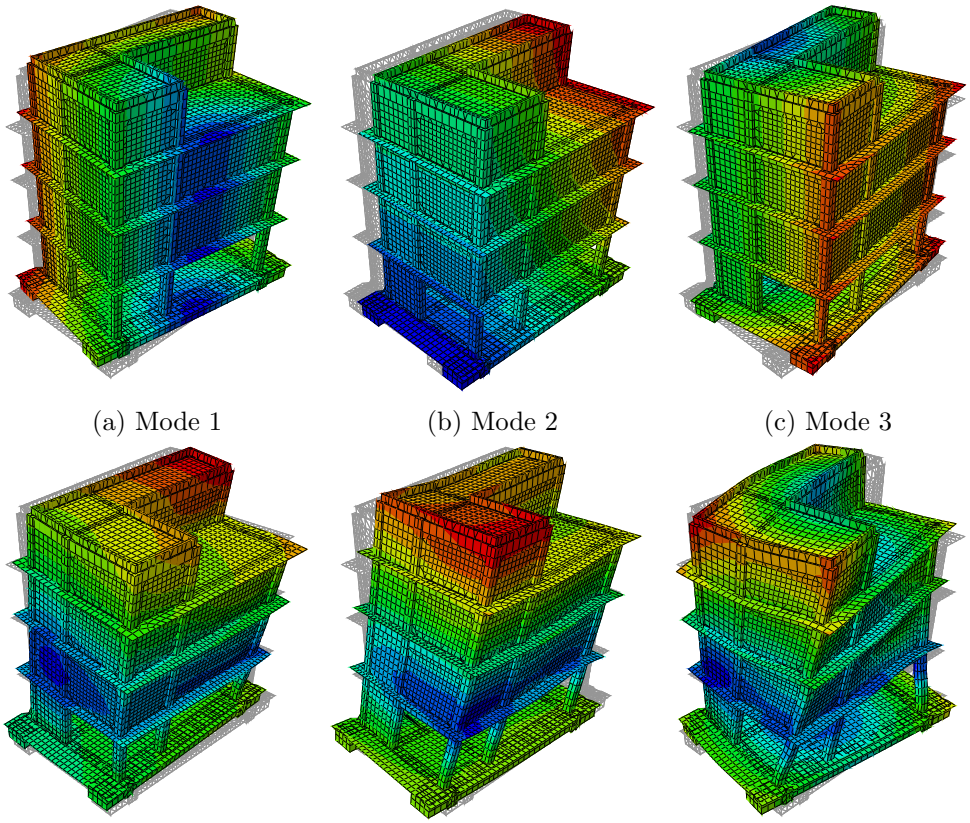

(a) Mode 1 (b) Mode 2 (c) Mode 3

(d) Mode 4 (e) Mode 5 (f) Mode 6

Figure 10: Mode shapes of the nominal FEM

enough motion that the forces from these devices are well-modeled as directionally-uncoupled).

- A simpler Case II groups superstructure elements composed of concrete with the same characteristic compressive strength (Table 4), each with a to-be-updated Young's modulus (3 parameters), and the same isolation-layer coefficients as in Case I (24 parameters).

- A more methodological Case III seeks to group parameters with similar

Table 4: Nominal compressive strength f'_{ck} and Young's modulus E_c, as well as the corresponding post-update Young's modulus E_c, for each superstructure concrete material

Nominal Compressive Strength f'_{ck} **[GPa]**	**Nominal Young's Modulus** E_c **[GPa]**	**Updated Young's Modulus** E_c **[GPa]**	**Superstructure Components**
36	32.78	34.42	elements in and below floor 0 (base)
27	29.15	30.61	elements above floor 0 and no higher than floor 3
21	25.85	27.14	elements above floor 3

(algebraically parallel) effects on the modal properties. The sensitivities of relative changes in the natural frequencies to relative changes in the parameters are first calculated. Then, parameters with negligible impact on the frequencies (those with sensitivity-matrix columns with two-norms less than 0.4%) are ignored. The remaining parameters are clustered together with others with *cosine distance* (Everitt et al., 2001) less than 0.05 via the "unweighted pair group parameter clustering method with arithmetic mean" (Shahverdi et al., 2009; Jang and Smyth, 2017a). Each of the resulting 31 groups of to-be-updated parameters was found to only include members from a single physically-motivated category used in Case II though not every group is from the same category (*i.e.*, Case III subdivides the groups in Case II).

Case I was found to lead to an easier match of modal properties, as expected, because it has a greater number of free parameters, but promotes excessive parameter changes that violate some clear underlying physical properties of the building; though the Case II–updated FEM slightly better predicted

time-history responses than Case I. Case II and Case III time-history responses were almost identical; thus, the simpler and physically-motivated clustering of Case II is used in the remainder of this paper.

The nominal superstructure concrete Young's moduli are chosen through interpolation of the relationship between concrete compressive strength f'_{ck} and the corresponding Young's modulus E_c provided by the Japanese concrete design code (Ueda, 2007) summarized in Table 5. This design code notes that, "in the case of repeated loading or when the applied stress level is low, the values in [Table 5] may be preferably increased by 10%" – thus, the concrete Young's moduli in Table 4 are interpolated from the compressive strength in the design drawings using the design code Table 5 and then multiplied by 110%. These moduli will be allowed to change by ±5% from their nominal values in the updating optimization.

Although the ALC panels have a Young's modulus of about 2 GPa, already much smaller than the other concrete elements, the installation allows some in-plane sliding between adjacent panels as well as out-of-plane rotation where connected to the main structure (beams and columns), so the effective stiffnesses of ALC panels are negligible compared with other concrete elements (in fact, a preliminary model updating that included the ALC panels'

Table 5: Relationship between characteristic compressive strength f'_{ck} and Young's modulus E_c in the Japanese concrete design code (Ueda, 2007)

f'_{ck} [GPa]	18	24	30	40
E_c [GPa]	22	25	28	31

effective Young's modulus resulted in an updated ALC Young's modulus that was more than three orders of magnitude smaller than those of the concrete elements — again, indicating the ALC plate effective moduli are negligible). Thus, while the panels are included in the modeling as placeholders in the event that future studies on ALC plates or other exterior wall panels — both deemed beyond the scope of this study — are needed, their stiffnesses herein are set to zero and their masses are applied to the adjacent main structural components.

In each horizontal direction, each isolation-layer device is modeled in low-level linear motion with a spring with a constant stiffness k and a viscous damper with a constant damping coefficient c (vertical flexibility is ignored). Thus, the restoring force at time t_l is approximated by

$$f(t_l) = kx(t_l) + c\dot{x}(t_l) \tag{1}$$

where $x(t_l)$ and $\dot{x}(t_l)$ are the displacement and velocity at time t_l, respectively, across the device. Combining (1) evaluated at N time points, $l = 1, 2, \ldots, N$, into a matrix equation results in

$$\underbrace{\begin{Bmatrix} f(1\Delta t) \\ f(2\Delta t) \\ \vdots \\ f(N\Delta t) \end{Bmatrix}}_{\mathbf{f}} = \underbrace{\begin{bmatrix} x(1\Delta t) & \dot{x}(1\Delta t) \\ x(2\Delta t) & \dot{x}(2\Delta t) \\ \vdots & \vdots \\ x(N\Delta t) & \dot{x}(N\Delta t) \end{bmatrix}}_{\mathbf{A} = [\mathbf{a}_k \;\; \mathbf{a}_c]} \begin{Bmatrix} k \\ c \end{Bmatrix} \tag{2}$$

Then, the least squares fit ($\hat{k}$, $\hat{c}$) for device parameters (k, c) can be calculated using the Moore-Penrose pseudoinverse of matrix $\mathbf{A}$; the resulting values $[\hat{k} \quad \hat{c}]^{\mathrm{T}} = \mathbf{A}^{\dagger}\mathbf{f}$, shown in Table 6, are used as the nominal device stiffness and damping coefficient. The restoring force prediction error, or residue, is $\mathbf{r} = \mathbf{A}[\hat{k} \quad \hat{c}]^{\mathrm{T}} - \mathbf{f}$. The average relative prediction error $err_{kc} = \|\mathbf{r}\|_2/\|\mathbf{f}\|_2$, where $\|\cdot\|_2$ denotes the vector two-norm, is also shown in Table 6. To determine how much the subsequent model updating will allow k and c to vary from their nominal initial values, define the residual $\mathbf{r}' = \mathbf{A}[\hat{k} + \Delta k \quad \hat{c} + \Delta c]^{\mathrm{T}} - \mathbf{f} = \mathbf{r} + \mathbf{a}_k \Delta k + \mathbf{a}_c \Delta c$ that results from stiffness Δk and damping Δc changes from nominal. The bounds on k are chosen to be the tightest range for which $\|\mathbf{r}'\|_2 = 1.5\|\mathbf{r}\|$ when Δc is zero, resulting in $\Delta k = \{-\mathbf{r}^{\mathrm{T}}\mathbf{a}_k \pm [(\mathbf{r}^{\mathrm{T}}\mathbf{a}_k)^2 + (1.5^2 - 1)\|\mathbf{a}_k\|_2^2\|\mathbf{r}\|_2^2]^{1/2}\}/\|\mathbf{a}_k\|_2^2$; if these two solutions are denoted Δk_+ and Δk_-, then the lower bound (LB) and upper bound (UB) are $\max\{0, \hat{k} + \Delta k_-\}$ (constrained so that the stiffness is never negative) and $\hat{k} + \Delta k_+$, respectively. The corresponding expression for Δc

Table 6: Nominal and updated stiffnesses and damping coefficients of isolation-layer devices

	RB1		**RB2**		**ESB1**		**ESB2**		**SDP1**		**SDP2**	
	x	y	x	y	x	y	x	y	x	y	x	y
$\hat{k}$ [kN/m]	1128	1104	1077	1115	1539	1413	1495	1453	3936	4070	4004	3772
LB	1062	1026	1016	1044	1367	1225	1022	1096	3634	3689	3634	3387
UB	1195	1182	1138	1187	1711	1602	1969	1810	4239	4452	4373	4157
updated k	1173	1044	1130	1165	1587	1571	1595	1349	3793	3709	3881	3995
$\hat{c}$ [Mg/s]	16.74	17.35	15.55	17.84	26.23	29.84	60.06	55.55	101.75	106.65	108.67	119.25
LB	15.88	0.00	1.36	1.17	0.00	0.00	0.00	0.00	30.84	19.15	22.08	30.06
UB	31.90	35.25	29.73	34.51	65.35	73.53	170.20	137.53	172.66	194.15	195.26	208.45
updated c	24.83	20.47	26.90	24.20	45.42	45.64	82.06	60.85	159.20	134.68	182.22	180.45
err_{kc} [%]	5.26	6.29	5.05	5.74	9.92	11.79	26.87	21.19	6.81	8.30	8.16	9.00

is identical except replacing "k" with "c" throughout. As will be seen in Section 6, constraining the isolation-layer coefficients within the resulting bounds, reported in Table 6, provides a high fidelity match.

5. Linear Updating and Mode Matching

Most model updating procedures result in optimization problems that minimize some cost (or objective) functions. Here, the error metric $J(\boldsymbol{\theta})$ is defined to be the sum of the error of each identified mode with the "matched" corresponding FEM mode:

$$J(\boldsymbol{\theta}) = \sum_{i \in \mathcal{I}^{\mathrm{ID}}} J_{i'_i i}(\boldsymbol{\theta}) \tag{3a}$$

where $\mathcal{I}^{\mathrm{ID}}$ is a set of experimentally identified mode numbers used in the optimization, i'_i is the FEM mode number matched to experimentally identified mode i, and $J_{i'_i i}(\boldsymbol{\theta})$ is a weighted sum of the relative differences between FEM mode i'_i and identified mode i:

$$\begin{aligned} J_{i'_i i}(\boldsymbol{\theta}) = & \quad \left| \hat{f}_{i'_i}(\boldsymbol{\theta}) - f_i \right| / f_i \\ & + \lambda_i^{\mathrm{MAC}} \left| 1 - \mathrm{MAC}\Big(\hat{\boldsymbol{\phi}}_{i'_i}(\boldsymbol{\theta}), \boldsymbol{\phi}_i \Big) \right| \\ & + \lambda_i^{\zeta} \quad \left| \hat{\zeta}_{i'_i}(\boldsymbol{\theta}) - \zeta_i \right| / \zeta_i \end{aligned} \tag{3b}$$

where f_i, $\boldsymbol{\phi}_i$ and ζ_i are the i^{th} experimentally identified natural frequency, mode shape and damping ratio, whereas $\hat{f}_{i'_i}(\boldsymbol{\theta})$, $\hat{\boldsymbol{\phi}}_{i'_i}(\boldsymbol{\theta})$ and $\hat{\zeta}_{i'_i}(\boldsymbol{\theta})$ are the corresponding values for the FEM's i'^{th}_i mode. The FEM mode number i'_i may be the same as the identified mode number i, but this is often not the

case because of FEM modes that remain unidentified from the experimental data (further discussed in the following section). This cost function uses the relative frequency and damping ratio differences so that all modes are evaluated on the same scale. $1 - \mathrm{MAC}(\hat{\boldsymbol{\phi}}_{i'_i}(\boldsymbol{\theta}), \boldsymbol{\phi}_i)$ quantifies the differences between the identified mode shape $\boldsymbol{\phi}_i$ and the FEM mode shape $\hat{\boldsymbol{\phi}}_{i'_i}(\boldsymbol{\theta})$.

λ_i^{MAC} and λ_i^{ζ} are weights that adjust the contribution to cost function (3) by errors from mode shapes and damping ratios, relative to those from the frequencies. Reducing relative frequency error and mode shape error are considered approximately of equal importance to ensure reproduction of structure time-history responses, so the mode shape weight λ_i^{MAC} is chosen to be unity for each mode i. The superstructure modes' damping ratios, which are sufficiently small to generate primarily monophase mode shapes, are of relatively little utility for matching those modes' frequencies and mode shapes; thus, the damping relative error weight λ_i^{ζ} is set to zero for superstructure modes $i \geq 4$. In contrast, because the isolation mode damping is much larger, with nonproportional complex mode shapes, accurate damping modeling in the isolation modes is essential for accurate response prediction, so $\lambda_i^{\zeta} = 1$ for modes $i = 1, 2, 3$; it should be noted that this could affect model updating accuracy if the identified damping ratios are poorly characterized, but including them here is essential since the modes 1–3 damping ratios — particularly modes 2–3 are complex and very nonproportional, so ignoring their damping and the complex nature of their mode shapes are more likely to lead to poor characterization of the isolation-layer behavior. Finally, the

superstructure modes are first updated using $\mathcal{I}_{\text{str}}^{\text{ID}} = \{4, 5, \ldots, 8\}$, and then the isolation modes using $\mathcal{I}_{\text{iso}}^{\text{ID}} = \{1, 2, 3\}$.

5.1. Mode Matching

With the cost functions defined, the next challenge is to find the FEM mode i_i' that corresponds to identified mode i. In other words, although there are 8 identified stable modes in Table 2, one must determine, for each identified mode, the FEM mode that corresponds: *i.e.*, similar frequency and mode shape. For example, stable identified mode 8 is found in Section 6 to not correspond to FEM mode 8, but rather FEM mode 9. This mismatch is expected: due to the limited number of measurement directions and/or locations, it is possible (perhaps even likely) that some modes of the experimental building cannot be identified; further, sensor noise can result in spurious non-physical modes appearing in the identification results.

When updating the parameters of the isolation-layer devices, mode matching is typically not a challenge because the number of identified modes and the number of FEM modes that can possibly be matched to them are both very small (three each), so there are only six possible match permutations, as shown in Figure 11. A cost function can be computed for each of the six scenarios, the smallest of which not only provides the updated parameters $\boldsymbol{\theta}$, but also indicates the best mode match.

In contrast, in the general case of n^{ID} identified modes, each to be matched to one of n^{FEM} modes (which likely does not constitute all FEM modes but rather those within a frequency range reasonably close to those of the iden-

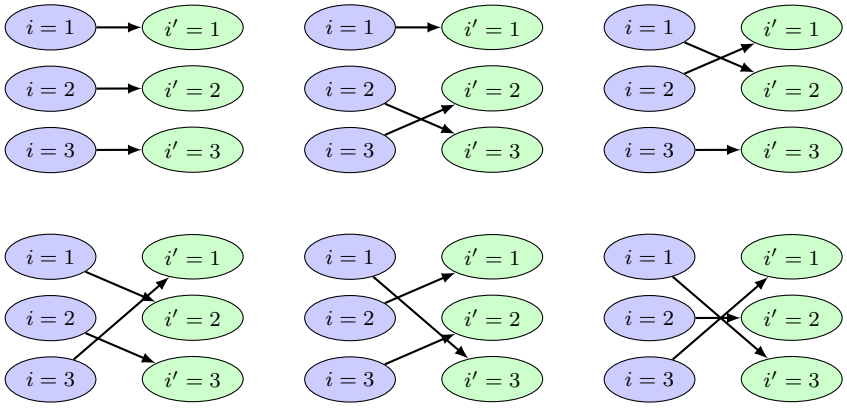

Figure 11: Possible mode matchings for the isolation-layer device parameter updating

tified modes), the number of permutations is $n^{\mathrm{FEM}}!/(n^{\mathrm{FEM}} - n^{\mathrm{ID}})!$, which is typically far too large for a tractable exhaustive search. For a particular choice of parameter vector $\boldsymbol{\theta}$, a modal analysis will provide a set of n^{FEM} candidate modal frequencies $\hat{f}_j(\boldsymbol{\theta})$ and corresponding mode shapes $\hat{\boldsymbol{\phi}}_j(\boldsymbol{\theta})$ for $j \in \mathcal{I}^{\mathrm{FEM}}$; for identifying the superstructure modes of the example herein, $\mathcal{I}^{\mathrm{FEM}} = \{j \,|\, \hat{f}_j(\boldsymbol{\theta}) \in [2, 17]\,\mathrm{Hz}\}$ because the modes below 2 Hz are the isolation modes, and the experimentally-identified modes only range up to about 17 Hz. Let $\mathcal{U}^{\mathrm{ID}} \subset \mathcal{I}^{\mathrm{ID}}$ and $\mathcal{U}^{\mathrm{FEM}} \subset \mathcal{I}^{\mathrm{FEM}}$ be the sets of yet unmatched experimentally-identified and FEM modes, respectively; when the mode-matching algorithm begins, these are identically $\mathcal{I}^{\mathrm{ID}}$ and $\mathcal{I}^{\mathrm{FEM}}$, respectively. Assume that the modes are numbered by increasing frequency; *i.e.*, $f_i < f_{i+1}$ and $\hat{f}_j(\boldsymbol{\theta}) < \hat{f}_{j+1}(\boldsymbol{\theta})$ for any positive i or j.

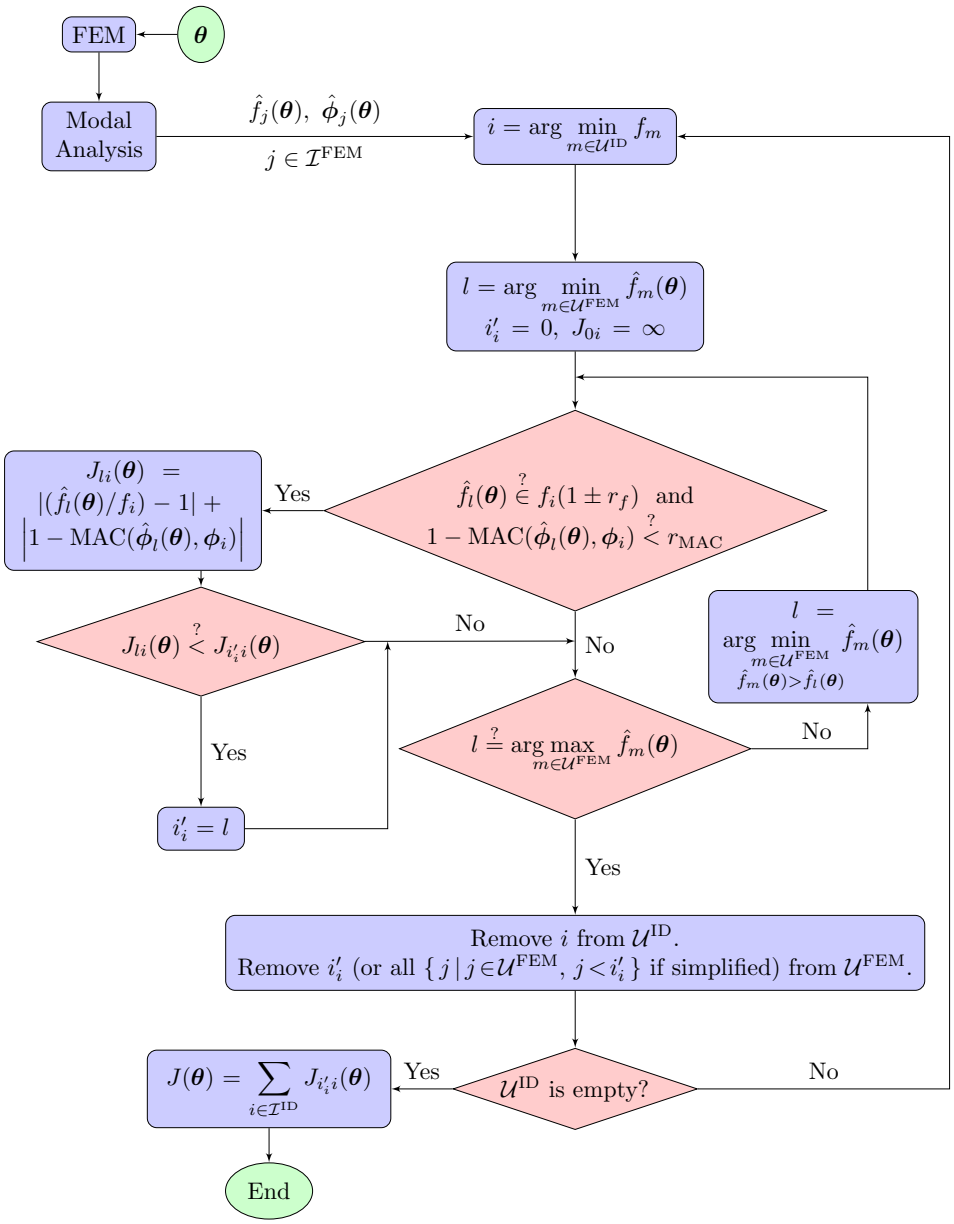

Figure 12: Flowchart for computing superstructure mode-matching cost function values (the damping ratio could be included but is omitted because λ_i^{ζ} is set to zero herein; elements drawn assuming λ_i^{MAC} is unity)

With these definitions, the mode-matching algorithm, depicted in Figure 12, proceeds as follows. First, choose the next identified mode yet to be matched; $i = \min_{m \in \mathcal{U}^{\text{ID}}} m$. Of all yet-unmatched FEM mode numbers $\mathcal{U}^{\text{FEM}}$, find those that have natural frequencies within a range around the identified modal frequency f_i and with mode shapes sufficiently similar, and set the i^{th} mode's contribution to the cost function $J(\boldsymbol{\theta})$ to be the minimum of the cost of each of those FEM modes; *i.e.*, let

$$\mathcal{U}_i^{\text{FEM}} = \left\{ l \mid l \in \mathcal{U}^{\text{FEM}}, \left| \frac{\hat{f}_l(\boldsymbol{\theta})}{f_i} - 1 \right| < r_f, \lambda_i^\zeta \left| \frac{\hat{\zeta}_l(\boldsymbol{\theta})}{\zeta_i} - 1 \right| < r_\zeta, \right. \\ \left. \lambda_i^{\text{MAC}} \left[1 - \text{MAC}(\hat{\boldsymbol{\phi}}_l(\boldsymbol{\theta}), \boldsymbol{\phi}_i) \right] < r_{\text{MAC}} \right\} \tag{4}$$

be the FEM mode numbers that potentially match identified mode i, where r_f, r_ζ and r_{MAC} denote the allowable levels of relative frequency deviation, relative damping ratio deviation times λ_i^ζ, and λ_i^{MAC} times the MAC metric deviation from a perfect mode shape match, respectively; herein, $r_f = 10\%$, r_ζ is not needed because λ_i^ζ is zero for superstructure mode matching, and $r_{\text{MAC}} = 15\%$. If $\mathcal{U}_i^{\text{FEM}}$ is an empty set, then $J_{i'_i i}(\boldsymbol{\theta}) = \infty$; otherwise, let $i'_i \in \mathcal{U}_i^{\text{FEM}}$ be the FEM mode number that provides the smallest cost and $J_{i'_i i}(\boldsymbol{\theta})$ be that smallest cost:

$$i'_i = \arg \min_{l \in \mathcal{U}_i^{\text{FEM}}(\boldsymbol{\theta})} J_{li}(\boldsymbol{\theta}) \tag{5}$$

Finally, remove FEM mode number i'_i from the unmatched $\mathcal{U}^{\text{FEM}}$, and remove identified mode number i from the unmatched $\mathcal{U}^{\text{ID}}$. Clearly, there is

no need to continue the algorithm if, at any stage, an identified mode's contribution $J_{i'_i i}(\boldsymbol{\theta})$ to the cost is infinite; otherwise, the cost $J(\boldsymbol{\theta})$ is calculated by summing the per-mode $J_{i'_i i}(\boldsymbol{\theta})$, $i \in \mathcal{I}^{\text{ID}}$.

Further, an optional simplification may be exploited if the modes are sufficiently spaced and the mode number matching is monotonic (which was found to be the case for the structure and experimental data herein); then, the algorithm can take a shortcut by restricting the search only to FEM modes with frequencies larger than those matched thus far; *i.e.*, at each stage (both initially and after each FEM mode is chosen to match an identified mode), $\mathcal{U}^{\text{FEM}} = \{\, l \mid l \in \mathcal{I}^{\text{FEM}},\ \hat{f}_l(\boldsymbol{\theta}) > \max_{i \in \mathcal{I}^{\text{ID}}, i \notin \mathcal{U}^{\text{ID}}} \hat{f}_{i'_i}(\boldsymbol{\theta}) \,\}$.

5.2. Optimization

To minimize the error metric $J(\boldsymbol{\theta})$, two optimization algorithms were evaluated: the Genetic Algorithm (GA) in the MATLAB® Global Optimization Toolbox and a Nelder Mead Simplex method via the `fminsearch` function in MATLAB® (a traditional hill climbing optimizer). For this optimization, the GA uses a population of 400 for 40 generations, with defaults for other parameters (5% elite rate, 80% crossover fraction, 1% mutation rate). When updating the superstructure parameters, no further tuning of the algorithm was needed. However, updating the isolation-layer parameters by directly minimizing $J(\boldsymbol{\theta})$ in (3) results in no value of $\boldsymbol{\theta}$ that is within the permissible range $[\boldsymbol{\theta}_{\text{LB}}, \boldsymbol{\theta}_{\text{UB}}]$ and also provides a "close" match, defined as satisfying all

of the following

$$\left|\hat{f}_{i'_i}(\boldsymbol{\theta}) - f_i\right| / f_i < 5\% \tag{6a}$$

$$\left|\hat{\zeta}_{i'_i}(\boldsymbol{\theta}) - \zeta_i\right| / \zeta_i < 5\% \tag{6b}$$

$$\left|1 - \mathrm{MAC}\left(\hat{\boldsymbol{\phi}}_{i'_i}(\boldsymbol{\theta}), \boldsymbol{\phi}_i\right)\right| < 5\% \tag{6c}$$

for every $i \in \mathcal{I}_{\text{iso}}^{\text{ID}}$ (if λ_i^{ζ} or λ_i^{MAC} were zero, which they are not herein for the isolation modes, the corresponding criterion would be ignored for a "close" match). To overcome this difficulty, the first 20 GA generations are devoted to finding a permissible $\boldsymbol{\theta}$ population that gives a "close" match; this is accomplished by instead minimizing a somewhat relaxed cost function

$$\begin{aligned}\tilde{J}(\boldsymbol{\theta}) = &\sum_{i \in \mathcal{I}_{\text{iso}}^{\text{ID}}} \max\left\{0,\ 0.05 - \left|\hat{f}_{i'_i}(\boldsymbol{\theta}) - f_i\right| / f_i\right\} \\ &+ \sum_{i \in \mathcal{I}_{\text{iso}}^{\text{ID}}} \lambda_i^{\text{MAC}} \max\left\{0,\ 0.05 - \left[1 - \mathrm{MAC}\left(\hat{\boldsymbol{\phi}}_{i'_i}(\boldsymbol{\theta}), \boldsymbol{\phi}_i\right)\right]\right\} \\ &+ \sum_{i \in \mathcal{I}_{\text{iso}}^{\text{ID}}} \lambda_i^{\zeta} \max\left\{0,\ 0.05 - \left|\hat{\zeta}_{i'_i}(\boldsymbol{\theta}) - \zeta_i\right| / \zeta_i\right\}\end{aligned} \tag{7}$$

that eventually converged to $\tilde{J}(\boldsymbol{\theta}) = 0$, indicating that the "close" criteria (6) were met. The remaining 20 generations, starting from the 20^{th} generation's population, minimized $J(\boldsymbol{\theta})$ to seek an even closer match.

The hill-climber failed to outperform the GA in the following respects. (a) As is typical, this hill-climber tended to get stuck at local minima and failed to search some key parts of the parameter space. (b) Hill-climbing optimizers, in general, offer only one solution to the problem; however, the

GA usually produces a population of solutions with extremely similar cost function values. In preliminary studies, one (or more) of the competing GA solutions outperformed the only solution obtained through the hill-climbing optimizer. (c) The GA is gradient-free and can minimize discontinuous cost functions. In this study, although cost function (3) seems to be smooth, it is indeed piecewise discontinuous due to the incorporation of the mode-matching decision process (Figure 11 or 12). Thus, $J(\boldsymbol{\theta})$ does not have finite gradients everywhere, which poses a problem for most hill-climbers. Thus, while preliminary studies evaluated the `fminsearch` hill-climber, it is subsequently omitted due to its inferior performance relative to the GA.

6. Results of Linear Model Updating

Figure 13 shows comparisons of the natural frequencies and mode shapes between the experimental building and the FEM before and after linear model updating; the natural frequencies of the identified and FEM modes are shown on the horizontal and vertical axes, respectively, as well as listed in Table 7. For most modes, the natural frequency errors have been reduced, especially for those with initially relatively large errors: the relative frequency differences for modes 4–6 reduce from 18%–29% to less than 1.5%. Further, after model updating, the identified mode shapes of modes 1–3 and mode 8 achieve much better matches with the corresponding FEM mode shapes. Since modes 1–3 (either identified or FEM) are the dominant modes for the horizontal motions, it should be expected that the dynamic behavior

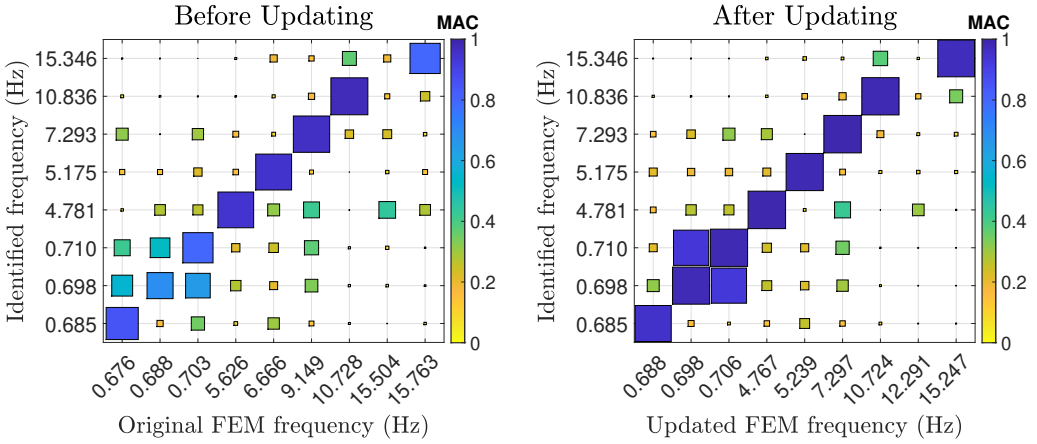

(a) Before linear model updating (b) After linear model updating

Figure 13: Comparisons of frequencies and mode shapes (MAC values) between experimentally identified modes and those from the (a) unupdated and (b) updated FEM models

Table 7: Frequency comparisons of the experimental building, and the original and updated FEMs

N4SID Identified		**Original FEM**			**Updated FEM**		
Mode #	**Freq. [Hz]**	**Mode #**	**Freq. [Hz]**	**(Err. [%])**	**Mode #**	**Freq. [Hz]**	**(Err. [%])**
1	0.685	1	0.676	(–1.352)	1	0.686	(0.174)
2	0.698	2	0.688	(–1.355)	2	0.700	(–0.376)
3	0.710	3	0.703	(–0.912)	3	0.702	(–1.051)
4	4.781	4	5.626	(17.668)	4	4.767	(–0.292)
5	5.175	5	6.666	(28.813)	5	5.240	(1.248)
6	7.293	6	9.149	(25.447)	6	7.296	(0.041)
7	10.836	7	10.728	(–1.000)	7	10.724	(–1.041)
		8	15.504	n/a	8	12.292	n/a
8	15.346	9	15.763	(2.540)	9	15.247	(–0.645)

of the updated FEM in the horizontal directions matches much more closely with those of the experimental building.

The effective masses (and moments of inertia) of the updated FEM's modes, computed by means of modal analysis, are listed in Table 8, where

Table 8: Effective mass and moment of inertia ratios of the FEM modes matched to identified modes 1–8

Identified Mode # (i)	**Matched FEM Mode # (i'_i)**	$\frac{M_i^x}{M_{\text{total}}}$	$\frac{M_i^y}{M_{\text{total}}}$	$\frac{M_i^z}{M_{\text{total}}}$	$\frac{I_i^x}{I_x}$	$\frac{I_i^y}{I_y}$	$\frac{I_i^z}{I_z}$
1	1	0.097	0.744	0.000	0.067	0.039	0.123
2	2	0.902	0.082	0.000	0.007	0.315	0.725
3	3	0.000	0.173	0.000	0.013	0.000	0.152
4	4	0.000	0.000	0.000	0.008	0.337	0.001
5	5	0.000	0.000	0.011	0.152	0.076	0.000
6	6	0.000	0.000	0.002	0.010	0.015	0.000
7	7	0.000	0.000	0.871	0.562	0.135	0.000
8	9	0.000	0.000	0.004	0.033	0.011	0.000
	$\sum_{i=1}^{8}$:	1.000	1.000	0.889	0.854	0.928	1.000

M_i^x, M_i^y and M_i^z are the effective masses of the i^{th} mode in the x, y, and z directions, respectively, and I_i^x, I_i^y and I_i^z are the effective moments of inertia of the i^{th} mode about the x, y, and z axes, respectively. The total mass M_{total} and the total moments of inertia of the FEM are readily available after constructing the FEM. For the x- and y-direction translations, as well as the rotation around the z axis, the sum of the effective masses (or moments of inertia) from the 8 listed modes are almost 100% of the total. For the z-direction translation, the FEM mode corresponding to the identified mode 7 has an effective mass as large as 87% of the total mass, making it the dominant mode for vertical motion. Further, the moments of inertia around the x and y axes, together, exceed 0.85 and 0.90, respectively. In sum, the FEM modes that are matched with the identified modes can capture the dominant dynamic behaviors of the experimental building.

The (updated) isolation-layer device damping coefficients provide some damping in both isolation and superstructure modes. The three isolation-

mode damping ratios are are now 0.0761, 0.0842 and 0.0788, which are only 0.29%, 2.34% and 0.45%, respectively, below those identified and reported in Table 2; since these errors are quite small, no additional modal damping is needed for isolation modes 1–3. However, the superstructure-mode damping ratios induced by the isolation-layer device linear viscous damping coefficients are quite small: 0.0079, 0.0066 and 0.0037 in modes 4–6 and effectively zero in all other superstructure modes. Thus, additional modal damping in modes 4–6 is added so that their total damping ratios match those reported in Table 2; *i.e.*, $0.0321-0.0079 = 0.0242$, $0.0341-0.0066 = 0.0275$ and $0.0317-0.0037 = 0.0280$, respectively. For mode 7, the updated model uses damping ratio 0.0414, taken from the Test 013 vertical mode identification in Table 3, which was found to well reproduce (and better than using Test 010's 0.0350 from Table 2) vertical motion in both the low-level random excitation and the stronger earthquake excitations. For modes 8 and up, the damping ratios are set to 0.0331, which is the average identified Test 010 superstructure mode damping ratio (*i.e.*, average of the damping ratios of modes 4–8 in Table 2).

To evaluate the effect of model updating on the time-history responses, the updated FEM is subjected to the random excitation in Test 010. While various implicit or explicit time integration algorithms could be used, a modal approach is used here, simulating the response of each of the first 36 modes (those less than 35 Hz) to a piecewise linear form of the 1 kHz-sampled table-center acceleration $\ddot{\mathbf{x}}_{\mathrm{g}}(t)$; the modal responses are then combined with the

mode shapes to provide the global response. For a measured experimental response $w(t)$ and the corresponding FEM prediction $\hat{w}(t;\boldsymbol{\theta})$, one metric of time-history relative prediction error is

$$Err_w^{\mathrm{RMS}}(\boldsymbol{\theta}) = \frac{|\mathrm{RMS}[\hat{w}(t;\boldsymbol{\theta})] - \mathrm{RMS}[w(t)]|}{\mathrm{RMS}[w(t)]} \times 100\% \tag{8}$$

where $\mathrm{RMS}[w(t)] = [t_{\mathrm{f}}^{-1} \int_0^{t_{\mathrm{f}}} w^2(t)\mathrm{d}t]^{1/2}$, or discrete time $[n_t^{-1} \sum_{k=0}^{n_t-1} w^2(k\Delta t)]^{1/2}$, is the root-mean-square response (RMS) over time $[0, t_{\mathrm{f}}]$.

Table 9 shows that the relative errors — using error metric (8) — in RMS acceleration responses in the x and y directions drop significantly, by about two thirds, after updating: from as much as 34.5% to at most 12.9% in the x direction, and from 26.9% to at most 8.0% in the y direction; the z-direction change is not as significant, but the vertical accelerations from the unupdated FEM were already more accurate than those in the x and y directions. Further, most of the relative errors in RMS forces in the x and y directions drop significantly after updating, with the largest among them

Table 9: Percentage errors, using metric (8), in acceleration response and isolation-layer device force RMSs using the linear FEM before (**after**) updating

Direc.	**Status**	**Errors* [%] in Acceleration RMS**	**Errors [%] in Isolation-Layer Device Force RMS**					
			RB1	**RB2**	**ESB1**	**ESB2**	**SDP1**	**SDP2**
x	before	7.3 – 34.5	13.8	31.0	13.3	26.7	16.9	16.7
x	(**after**)	**(0.2 – 12.9)**	**(2.9)**	**(6.1)**	**(6.4)**	**(1.4)**	**(10.5)**	**(9.8)**
y	before	9.2 – 26.9	9.9	14.8	14.1	7.8	9.8	14.5
y	(**after**)	**(0.3 – 8.0)**	**(4.4)**	**(2.3)**	**(8.2)**	**(7.8)**	**(7.7)**	**(4.0)**
z	before	0.0 – 8.5	n/a	n/a	n/a	n/a	n/a	n/a
z	(**after**)	**(1.0 – 7.5)**	**(n/a)**	**(n/a)**	**(n/a)**	**(n/a)**	**(n/a)**	**(n/a)**

* minimum and maximum errors across the 14 structure accelerometers

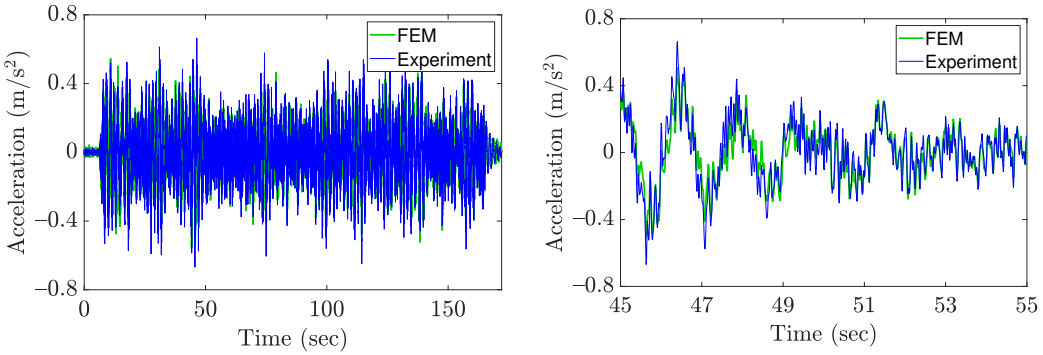

(a) x-direction acceleration (b) Zoomed-in version

Figure 14: Measured and calibrated-FEM-predicted accelerations, both downsampled to 100 Hz, from the accelerometer near grid 1A at floor 0 (base) in random excitation Test 010: (a) full time duration; (b) narrower time window to show detailed comparison

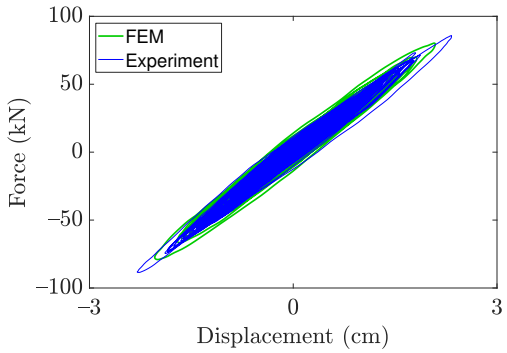

Figure 15: Measured force-displacement loops, and those predicted by the entire updated linear FEM, of the SDP1 in the x direction in random excitation Test 010

also dropping by more than two thirds.

The acceleration response with the largest relative error in RMS, the x-direction acceleration at the base-level sensor near grid 1A on Figure 2, is shown in Figure 14, both as measured (and downsampled to 100 Hz) and as predicted with the updated FEM (similar graphs for the responses with smaller prediction errors, omitted for brevity, exhibit FEM predicted accelerations that look almost exactly the same as those measured). Even for this

worst case, the acceleration time history from the experiment is still fairly well reproduced.

Figure 15 shows a comparison of the simulated and the measured force-displacement loops for the SDP1 in the x direction; even though this force exhibits the largest prediction error among all restoring forces, visual inspection shows that the equivalent linear stiffness and damping of the measured restoring force are sufficiently represented by the linear simulation.

7. Formulation of the Partially Nonlinear FEM

The rubber bearings exhibited slight stiffness reductions during large earthquake-induced displacements, so linear models are close but not perfect for modeling their behavior; a directionally uncoupled bilinear model is utilized herein. Models of the two elastic sliding bearings and the two metallic-yielding steel damper pairs were developed in a previous study (Brewick et al., 2020) based on the responses during Test 016 (Tohoku) and are mildly suboptimal during random excitations, primarily due to insufficient damping. Thus, slightly different ESB and SDP models are developed in this section. Then, the methodology for coupling the nonlinear isolator models with the updated linear superstructure model is provided, followed by an evaluation of the time-history predictions of the combined building model.

7.1. Modeling the Isolation-Layer Devices

As exemplified in Figure 6, the RBs behaved linearly in each of the x and y directions under random excitations (Tests 010–012); linear regression of the

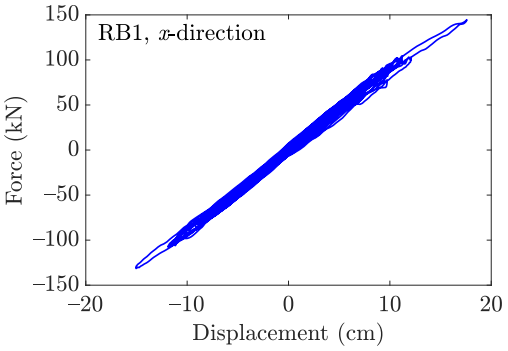

Figure 16: RB1 x-direction force-displacement loops in Test 016

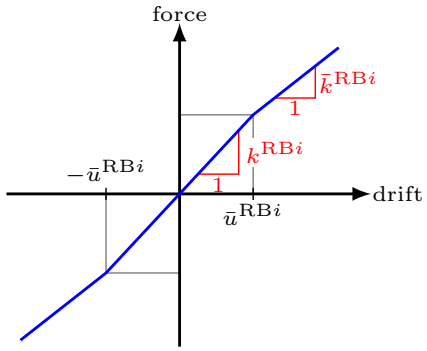

Figure 17: Rubber bearing bilinear elastic stiffness model

force-displacement data estimates stiffnesses of approximately 1100 kN/m. During the earthquake excitations (Tests 013–016), the RBs also appear quite linear, but a linear regression of Test 016 force-displacement data (Figure 16) estimates stiffnesses of approximately 950 kN/m, indicating some stiffness reduction when the displacement is large. Thus, RBi ($i \in \{1, 2\}$) is modeled herein with two uncoupled identical bilinear elastic stiffness elements — as depicted in Figure 17 with initial stiffnesses $k^{\mathrm{RB}i} = k_{xx}^{\mathrm{RB}i} = k_{yy}^{\mathrm{RB}i}$, postyield stiffnesses $\bar{k}^{\mathrm{RB}i} = \bar{k}_{xx}^{\mathrm{RB}i} = \bar{k}_{yy}^{\mathrm{RB}i}$, and yield displacement $\bar{u}^{\mathrm{RB}i} = \bar{u}_x^{\mathrm{RB}i} = \bar{u}_y^{\mathrm{RB}i}$ — in parallel with the linear viscous damping coefficients $c_{xx}^{\mathrm{RB}i}$ and $c_{yy}^{\mathrm{RB}i}$ found in the previous section and reported in Table 6. Thus, RBi's force in the x direction is given by

$$\begin{aligned} \hat{f}_x^{\mathrm{RB}i} &= k^{\mathrm{RB}i} u_x^{\mathrm{RB}i} + c_{xx}^{\mathrm{RB}i} \dot{u}_x^{\mathrm{RB}i} \\ &\quad + (k^{\mathrm{RB}i} - \bar{k}^{\mathrm{RB}i})(u_x^{\mathrm{RB}i} + \bar{u}^{\mathrm{RB}i})[1 - H(u_x^{\mathrm{RB}i} + \bar{u}^{\mathrm{RB}i})] \\ &\quad + (k^{\mathrm{RB}i} - \bar{k}^{\mathrm{RB}i})(u_x^{\mathrm{RB}i} - \bar{u}^{\mathrm{RB}i}) H(u_x^{\mathrm{RB}i} - \bar{u}^{\mathrm{RB}i}) \end{aligned} \tag{9}$$

where $H(\cdot)$ is the Heaviside unit step function; the formula for the y-direction force is identical by replacing every x with y.

The ESBs and SDPs, which exhibit clear hysteretic behavior in all of the tests, are each modeled using a bidirectionally coupled (unlike in the linear model calibrated based on motion sufficiently small that no directional coupling is needed) Bouc-Wen hysteretic behavior of the form (Park et al., 1986)

$$\dot{Z}_x = A\dot{u}_x - \beta\left|\dot{u}_x Z_x\right| Z_x - \gamma\dot{u}_x Z_x^2 - \beta\left|\dot{u}_y Z_y\right| Z_x - \gamma\dot{u}_y Z_x Z_y \tag{10a}$$

$$\dot{Z}_y = A\dot{u}_y - \beta\left|\dot{u}_y Z_y\right| Z_y - \gamma\dot{u}_y Z_y^2 - \beta\left|\dot{u}_x Z_x\right| Z_y - \gamma\dot{u}_x Z_x Z_y \tag{10b}$$

where u_x and u_y are the relative displacements across the device in the x and y directions, respectively, and A, β and γ control the shape of the hysteresis. The two SDPs have nearly identical behavior but the two ESBs act somewhat differently from each other (Brewick et al., 2020); thus, the SDPs are assumed to have identical parameters, but the ESB1 and ESB2 parameters are allowed to differ. The resulting ESB and SDP model forces are then provided by

$$\begin{Bmatrix} \hat{f}_x^{\mathrm{ESB}i} \\ \hat{f}_y^{\mathrm{ESB}i} \end{Bmatrix} = \mu_{\mathrm{ESB}i}(t) W_{\mathrm{ESB}i}(t) \begin{Bmatrix} Z_x^{\mathrm{ESB}i} \\ Z_y^{\mathrm{ESB}i} \end{Bmatrix} + \begin{Bmatrix} c_{xx}^{\mathrm{ESB}i}\dot{u}_x^{\mathrm{ESB}i} \\ c_{yy}^{\mathrm{ESB}i}\dot{u}_y^{\mathrm{ESB}i} \end{Bmatrix} \tag{11a}$$

$$\begin{Bmatrix} \hat{f}_x^{\mathrm{SDP}i} \\ \hat{f}_y^{\mathrm{SDP}i} \end{Bmatrix} = \mathbf{K}^{\mathrm{SDP}} \left[\alpha \begin{Bmatrix} u_x^{\mathrm{SDP}i} \\ u_y^{\mathrm{SDP}i} \end{Bmatrix} + (1-\alpha) \begin{Bmatrix} Z_x^{\mathrm{SDP}i} \\ Z_y^{\mathrm{SDP}i} \end{Bmatrix} \right] + \begin{Bmatrix} c_{xx}^{\mathrm{SDP}i}\dot{u}_x^{\mathrm{SDP}i} \\ c_{yy}^{\mathrm{SDP}i}\dot{u}_y^{\mathrm{SDP}i} \end{Bmatrix} \tag{11b}$$

$\mu_{\mathrm{ESB}i}(t) = \mu_0[S^{-1}W_{\mathrm{ESB}i}(t)\cdot(\mathrm{mm}^2/\mathrm{N})]^{\mu_1}[V^{\mathrm{ESB}i}(t)\cdot(\mathrm{s/mm})]^{\mu_2}$ is the coefficient of friction, where $S = 0.1018\,\mathrm{m}^2$ is the slider's effective surface area, $W_{\mathrm{ESB}i}(t)$

is the weight carried by ESBi at time t, $V^{\mathrm{ESB}i}(t) = \|[\dot{u}_x^{\mathrm{ESB}i}(t) \quad \dot{u}_y^{\mathrm{ESB}i}(t)]\|_2$ is the sliding velocity, and the friction formula coefficients are $\mu_0 = 0.0606$, $\mu_1 = -0.5883$ and $\mu_2 = 0.1148$ as determined in Brewick et al. (2020); $\mathbf{K}^{\mathrm{SDP}} = \left[[k_{xx}^{\mathrm{SDP}} \quad k_{xy}^{\mathrm{SDP}}]^{\mathrm{T}} \quad [k_{xy}^{\mathrm{SDP}} \quad k_{yy}^{\mathrm{SDP}}]^{\mathrm{T}}\right]$ is a symmetric SDP stiffness matrix; α defines the SDP postyield-to-preyield stiffness ratio; and $c_{xx}^{(\cdot)}$ and $c_{yy}^{(\cdot)}$ are damping coefficients in x and y directions, respectively (which are not fixed at the linear model's values in Table 6 but rather subsequently optimized).

Several metrics $\mathcal{M}_{(\cdot)}$ can be used to evaluate the fidelity of a single isolation-layer device model or of a set of device models. Metric $\mathcal{M}_{\hat{f}(t,u(t))}$: The model error for a single device can be quantified by the mean square error between the measured device forces' time histories and those predicted using the device model in (9) or (10)–(11) driven by the measured cross-device drifts and drift velocities; this metric is defined mathematically in (A.1) in Appendix A. Metric $\mathcal{M}_{\hat{f}(t;\boldsymbol{\theta},\ddot{\mathbf{x}}_{\mathrm{g}})}$: The force response errors for a candidate set of models for the devices are computed by simulating the response of a partially nonlinear FEM (linear FEM coupled with candidate models of the isolation-layer devices) to the measured shake table accelerations, extracting the resulting device force time histories, and quantifying the relative errors in the forces' RMS using (8). Metric $\mathcal{M}_{\hat{\zeta}}$: Modal damping evaluation is determined for a candidate set of models for the devices by comparing the measured responses' identified modal damping in Section 3 with the effective model damping estimated, using the same system identification strategy, from the 42 acceleration time-history responses of a partially nonlinear FEM

at the 14 accelerometer locations.

Preliminary studies showed that omitting the linear viscous terms in (11) leads to isolation-mode damping ratios computed from time-history responses to low-level random excitations such as Test 010 ($\mathcal{M}_{\hat{\zeta}}$) that are up to about a quarter smaller than those identified and reported in Table 2. Further, straightforward optimization of the ESB and SDP parameters in (10)–(11) to match the experimental force-displacement relationships in Tests 010 and 016 (*i.e.*, minimizing $\mathcal{M}_{\hat{f}(t,u(t))}$) still does not lead to sufficient levels of damping ($\mathcal{M}_{\hat{\zeta}}$). Finally, the RB parameters in (9) that minimize the mean square RB force prediction error ($\mathcal{M}_{\hat{f}(t,u(t))}$) do not consistently lead to smaller errors in simulated RB force RMS ($\mathcal{M}_{\hat{f}(t;\boldsymbol{\theta},\ddot{\mathbf{x}}_{\mathrm{g}})}$); rather, slightly different RB parameters that are very mildly suboptimal in reducing mean square RB force error ($\mathcal{M}_{\hat{f}(t,u(t))}$) can provide smaller simulated RB force RMS ($\mathcal{M}_{\hat{f}(t;\boldsymbol{\theta},\ddot{\mathbf{x}}_{\mathrm{g}})}$). To address these trade offs, a two-level hierarchical optimization strategy — detailed in Appendix A — is used to introduce sufficient damping in low-level response and balance trade offs between local device-specific model fidelity and that of the overall partially nonlinear FEM. The resulting isolation-layer device parameters are listed in Table 10.

It may be noted that the optimal parameters for the two ESBs are quite different from each other, and the damping coefficients for ESB1 in the two horizontal directions differ significantly as well. This is not surprising given that ESB1 was seen to exhibit a strong stick-slip behavior that was quite different from ESB2 (Brewick et al., 2020). Further, the SDP Bouc-Wen

Table 10: Parameters in the RB, ESB and SDP models

Parameter	RB1	RB2	ESB1	ESB2	SDP
k_{xx}	**1.075 MN/m**	**1.025 MN/m**			**3.975 MN/m**
k_{yy}	**1.075 MN/m**	**1.025 MN/m**			**3.779 MN/m**
k_{xy}	0	0			0
$\bar{k}$	**0.786 MN/m**	**0.772 MN/m**			
$\bar{u}$	**0.0258 m**	**0.0309 m**			
c_{xx}	24.83 Mg/s	26.90 Mg/s	**3.79 Mg/s**	**30.00 Mg/s**	**90.00 Mg/s**
c_{yy}	20.47 Mg/s	24.20 Mg/s	**50.04 Mg/s**	**20.00 Mg/s**	**90.00 Mg/s**
A			*47.13* m^{-1}	*54.10* m^{-1}	1
β			**10.41** $\mathbf{m^{-1}}$	**25.41** $\mathbf{m^{-1}}$	**635** $\mathbf{m^{-2}}$
γ			**36.72** $\mathbf{m^{-1}}$	**28.69** $\mathbf{m^{-1}}$	**1102** $\mathbf{m^{-2}}$
α					**0.1225**

Bold indicates optimized parameters; *italic* indicates parameters computed from optimized parameters; other parameters are fixed.

parameters here differ mildly from those reported in Brewick et al. (2020), which optimized solely for local device behavior in Test 016; the parameters here generalize better to the random excitation response in Test 010 as well as the lower-level earthquake response in Test 013 (which exhibited larger postyield SDP stiffnesses, possibly because of smaller motion than in Test 016 or because the SDP stiffnesses degraded in Tests 013–015).

7.2. Time-History Analysis

The linear superstructure is combined with the nonlinear isolation-layer device models to simulate the time-history responses of the building; the resulting equation of motion is:

$$\mathbf{M}\ddot{\mathbf{x}} + \mathbf{C}\dot{\mathbf{x}} + \mathbf{K}\mathbf{x} = -\mathbf{M}\mathbf{P}\ddot{\mathbf{x}}_{\mathrm{g}} + \mathbf{K}_{\mathrm{iso}}^{\mathrm{nom}}\mathbf{x}_{\mathrm{iso}} - \mathbf{B}_{\mathrm{iso}}\,\mathbf{f}_{\mathrm{iso}}(\mathbf{x}_{\mathrm{iso}}, \dot{\mathbf{x}}_{\mathrm{iso}}) \qquad (12)$$

where $\mathbf{M}$, $\mathbf{C}$ and $\mathbf{K}$ are the $n \times n$ (n is the number of DOFs) global mass, damping and stiffness matrices of the updated linear FEM, in which $\mathbf{M}$ remains unchanged throughout this study, $\mathbf{C}$ represents the damping in the

superstructure (computed from the added modal damping discussed in Section 6) and the linear viscous damping in the isolation layer, and $\mathbf{K}$ is the updated linear stiffness matrix; $\mathbf{P}$ is an $n\times 6$ influence matrix for the 6×1 ground (shake table center) excitation vector $\ddot{\mathbf{x}}_{\mathrm{g}}$; $\mathbf{x}$ is a vector of nodal displacements relative to the shake table; $\mathbf{x}_{\mathrm{iso}} = \mathbf{G}_{\mathrm{iso}}\mathbf{x}$ is a vector of isolation-layer device drifts relative to the shake table ($\mathbf{G}_{\mathrm{iso}}$ is a transformation matrix extracting these drifts from the vector of all displacements); $\mathbf{K}_{\mathrm{iso}}^{\mathrm{nom}}$ is a stiffness matrix that cancels out the nominal linear isolation-layer restoring forces (from the updated linear FEM) so that the actual nonlinear restoring forces can be included as $-\mathbf{B}_{\mathrm{iso}}\,\mathbf{f}_{\mathrm{iso}}(\mathbf{x}_{\mathrm{iso}}, \dot{\mathbf{x}}_{\mathrm{iso}})$, where $\mathbf{f}_{\mathrm{iso}}(\mathbf{x}_{\mathrm{iso}}, \dot{\mathbf{x}}_{\mathrm{iso}})$ is a vector of isolation-layer device restoring forces that depend on $\mathbf{x}_{\mathrm{iso}}$ and $\dot{\mathbf{x}}_{\mathrm{iso}}$ and $\mathbf{B}_{\mathrm{iso}}$ is an influence matrix that reintroduces $\mathbf{f}_{\mathrm{iso}}(\mathbf{x}_{\mathrm{iso}}, \dot{\mathbf{x}}_{\mathrm{iso}})$ back into the global force vector.

The advantages of this formulation are three-folded. First, the left-hand side of (12) remains linear, so the modal superposition method remains applicable. Since the experimental data is low-pass filtered at 35 Hz, modes with frequencies above 35 Hz can be neglected, reducing the 84,669 DOFs down to 36 modal DOFs. Second, regardless of the excitation, the eigenvalues and eigenvectors of the dynamic system remain unchanged, so modal decomposition need be performed only once. Third, since the restoring forces of the rubber bearings, elastic sliding bearings and the U-shape steel damper pairs are introduced as external forces in this formulation, different models of the isolation-layer devices can be easily incorporated into this formulation only by changing the form of $\mathbf{f}_{\mathrm{iso}}(\mathbf{x}_{\mathrm{iso}}, \dot{\mathbf{x}}_{\mathrm{iso}})$ on the right-hand side, instead of mak-

ing extensive changes to the structural system (the left-hand side), which is a benefit in the subsequent studies.

Utilizing (12), the partially nonlinear model's time-history responses to the earthquake excitation from Test 013 are computed and compared with the experimentally measured responses (note that Test 013 is intentionally chosen here as it was not used in calibrating the isolation-layer devices); relative errors in RMS are shown in Table 11. The z-direction accelerations are very well reproduced, indicating that the superstructure FEM is well constructed and updated; the small discrepancies are likely due to approximations in constructing the FEM. The slightly lower fidelity of the x- and y-direction predicted accelerations could result from the limitations of the bidirectional Bouc-Wen model of the isolation layer that cannot model the stick-slip behavior of the ESB1 (especially in the x direction) observed in this study (Brewick et al., 2020), as exhibited by the larger error in RMS x-direction ESB1 restoring forces. The unmodeled stick-slip behavior also affects the y-direction restoring forces due to the rotation of the building. The rubber bearing restoring forces are better reproduced than those of the

Table 11: Percentage errors, using metric (8), in acceleration response and isolation-layer device force RMSs using the partially nonlinear system model

Direction	**Errors* [%] in Acceleration RMS**	**Errors [%] in Isolation-Layer Device Force RMS**					
		RB1	**RB2**	**ESB1**	**ESB2**	**SDP1**	**SDP2**
x	1.4 – 11.4	11.2	5.4	23.8	9.6	2.1	0.2
y	3.6 – 9.7	9.9	8.0	7.3	11.7	2.1	5.5
z	2.5 – 6.8	n/a	n/a	n/a	n/a	n/a	n/a

* minimum and maximum errors across the 14 structure accelerometers

ESBs due to accurate estimation of the stiffnesses; the SDP restoring forces are reproduced very accurately, with errors in RMS at most a few percent.

Figure 18 shows comparisons of the accelerations on floor 0 at the sensor

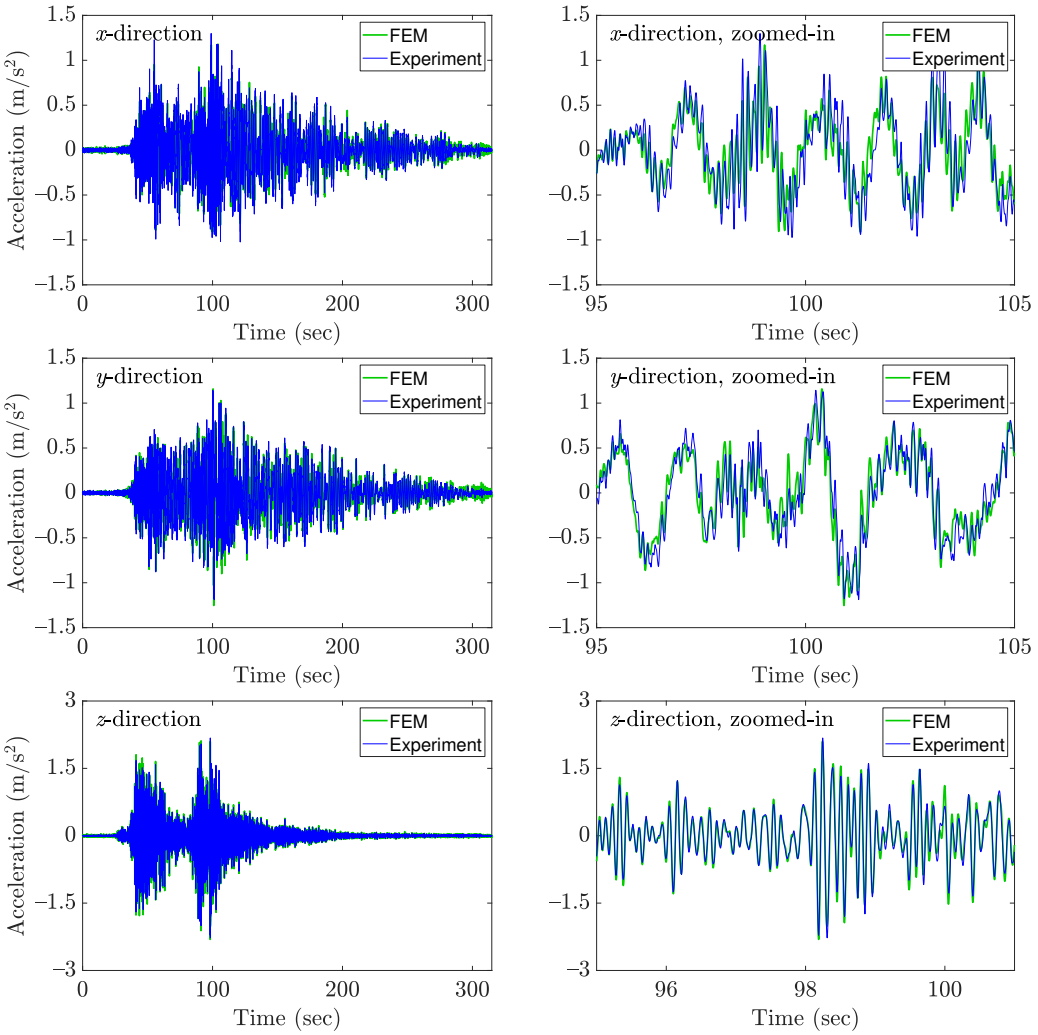

Figure 18: Measured and calibrated-FEM-predicted accelerations from the accelerometer near grid 1A on floor 0 in Test 013 (scaled Tohoku-Oki earthquake): the left graphs show the full time duration; the right graphs show a narrower time window to show detailed comparison (note: the right z-direction graph uses a narrower time window to show the detail for the higher-frequency vertical motion)

near grid 1A on Figure 2: the x-direction response measured by this sensor had the largest relative errors in RMS prediction (11.4% as shown in Table 11). In the x and y directions, the large responses (*e.g.*, around 50 and 100 sec) are reproduced well, with a very good match in terms of magnitudes and frequencies. Visual inspection shows that the y-direction response is reproduced slightly better than the x-direction response. The z-direction response is simulated very well, which is typical for all responses in this direction, and the slight differences may be due to small differences in damping for modes with vertical motion. Further, the good matches of accelerations in all three directions indicate that a linear superstructure model is sufficient, which is consistent with the intent of typical base-isolation design.

As observed in Figure 19, the stiffnesses of the RB bilinear model match those from the experimental tests in both directions. For the elastic sliding bearings and the steel damper pairs, the restoring forces generated by the modified Bouc-Wen models match well the experimental data in terms of slopes and outer loop excursions (perfect matches cannot be obtained due to the irregular stick-slip behavior of ESB1, which poses greater modeling challenges beyond the scope of this study).

8. Conclusions and Future Work

To leverage the data from the expensive full-scale seismic tests conducted on 8 August 2013 at Japan's E-Defense facility to be used for future investigations on new seismic protective designs, controllable damping strate-

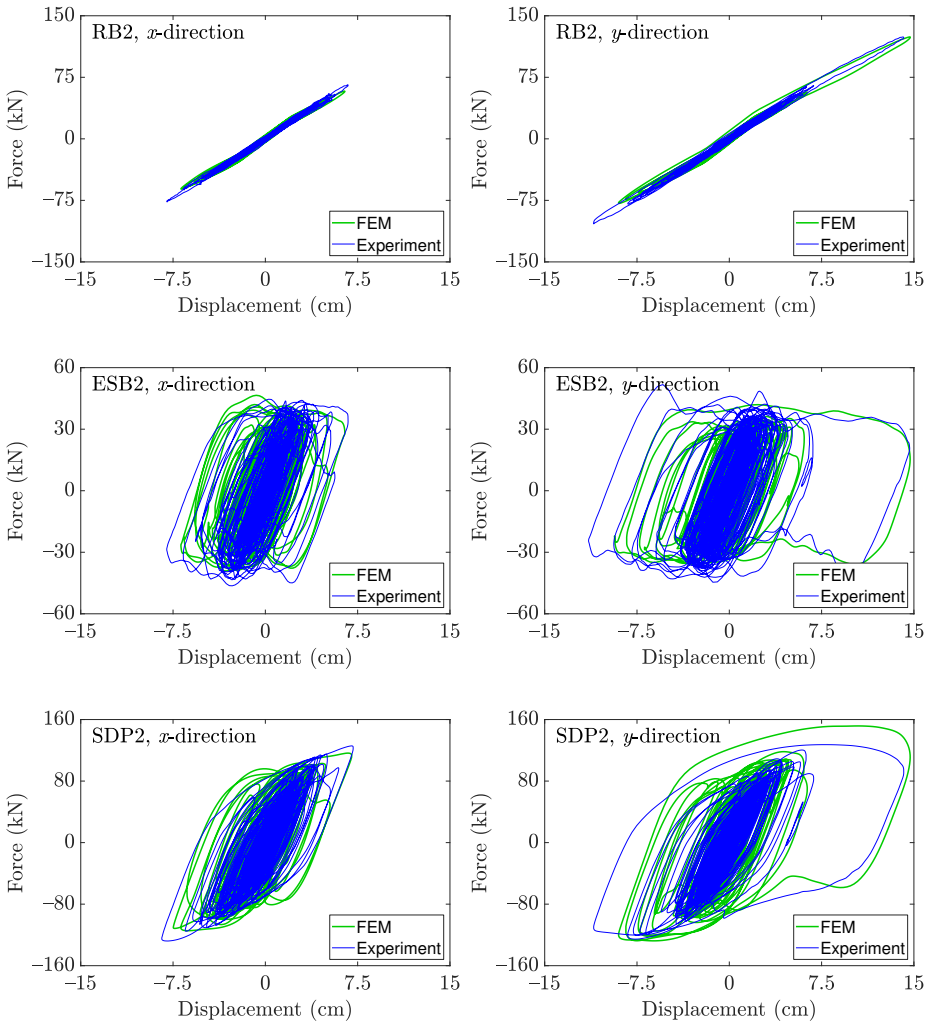

Figure 19: Measured and calibrated-FEM-predicted force-displacement loops during the scaled Tohoku-Oki Test 013

gies, retrofit procedures, and so forth, FEMs were assembled based on the structural design drawings, updated to have approximately the same modal properties as the experimental building, and combined with optimal nonlinear models of the isolation-layer devices to reproduce the responses of the

building under earthquake excitations. Insights gained through this study are listed as follows.

1. For a generic type of base-isolated structures resembling the one in this study, the modes can be separated into isolation modes and superstructure modes. Superstructure linear stiffness changes have minor effects on the frequencies and mode shapes of the isolation modes, and vice versa. Further, the superstructure damping has a negligible effect on the damping ratios of the isolation modes. Finally, the superstructure modes are approximately proportionally damped, while the isolation modes are not.
2. A mode-matching algorithm was proposed to efficiently match the experimental modes with the corresponding FEM modes, by searching for FEM modes with modal properties resembling those of the to-be-matched experimental mode and choosing the one leading to the smallest deviation in modal characteristics.
3. To reduce the computational burden of base-isolated building model updating and based on the insight gained in #1, two stages for linear model updating are proposed, in which the superstructure linear stiffnesses are first updated so that the superstructure modes' natural frequencies and mode shapes of the experimental building match those of the FEM; then, the isolation-layer stiffnesses and damping coefficients are updated so that the isolation modes' natural frequencies, damping ratios and mode shapes match. The modal properties of

the unupdated and updated FEMs were compared with those from the experiment; better agreement after model updating demonstrated the proposed approach successful. The matched modes' effective masses (moments of inertia), relative to the total mass (total moments of inertia), indicated that the matched modes capture the major dynamic properties of the building in all six DOFs. This conclusion was echoed by the good match between the simulated time-history responses using the updated FEM and those from the experimental data.

4. A final partially nonlinear FEM is determined by combining the updated superstructure FEM, rubber bearings modeled with directionally uncoupled bilinear stiffness models with a constant damping coefficient in each horizontal direction, and elastic sliding bearings and steel damper pairs modeled with bidirectionally coupled Bouc-Wen models with constant damping coefficients in each horizontal direction. Updating the models of the isolation-layer devices required: (a) adding viscous damping to better capture their behavior, and the resulting energy dissipation, in low-level excitation; (b) the linear stiffnesses of the steel damper pairs, when calibrated from the larger seismic responses alone, are a bit too small to be faithful to the response in the low-level motion, so optimizing using both excitations is necessary for a generic model that spans the excitation levels. This combined model satisfactorily reproduced the nonlinear time-history responses of the experimental building, thereby validating the practical applicability

of proposed isolation-layer device models and alleviating the research community's dearth of numerical experimentally-calibrated models for full-scale base-isolated buildings with lateral-torsional coupling effects.

Future work that is beyond the scope of this study includes: quantifying the uncertainty in parameter estimates (natural frequencies, damping ratios and mode shapes) identified from N4SID method and their propagation into the FEM parameter updating; model updating using only acceleration responses (and possibly limited sensing of isolation-layer drift) as in a real structure and exploring a fully-coupled model updating; developing nonlinear models of the superstructure for use in simulating extreme seismic events; testing novel control strategies, *e.g.*, neural network accelerated hybrid model predictive control (Yu and Johnson, 2022b); and validation of novel model updating approaches, *e.g.*, CTLS-based CMCM model updating method (Yu and Johnson, 2022a). The updated partially nonlinear FEM will be made open source and, together with an accompanying documentation, will be posted on the Natural Hazards Engineering Research Infrastructure (NHERI) repository (see Appendix B).

Acknowledgments

This material is based upon work supported by the National Science Foundation (NSF) under grants 13-44937/13-44622 and 16-63667; any opinions, findings, and conclusions or recommendations expressed in this material are those of the authors and do not necessarily reflect the views of the NSF.

The first and third authors gratefully acknowledge the support of a Provost's Fellowship and a Viterbi Postdoctoral Fellowship, respectively, from the University of Southern California, as well as the efforts of Dr. Wael M. Elhaddad in packaging the experimental data.

Appendix A. Two-Level Strategy for Optimizing Isolation-Layer Device Parameters

To optimize the isolation-layer device parameters for the locally nonlinear FEM, a two-level hierarchical strategy is used. For each isolation-layer device D, the first level of the strategy selects a set of candidate values for a subset of the device parameters (or their bounds) and then, for each candidate subset, optimizes the other device parameters using a cost metric E_D:

$$E_D(\boldsymbol{\theta}_D) = E_D^{(\text{Test 010})}(\boldsymbol{\theta}_D) + E_D^{(\text{Test 016})}(\boldsymbol{\theta}_D) \tag{A.1a}$$

$$E_D^{(T)}(\boldsymbol{\theta}_D) = \left[\frac{\sum_{k=0}^{n_t-1} [\hat{f}_x^D(k\Delta t;\boldsymbol{\theta}_D) - f_x^D(k\Delta t)]^2 + [\hat{f}_y^D(k\Delta t;\boldsymbol{\theta}_D) - f_y^D(k\Delta t)]^2}{\sum_{k=0}^{n_t-1} [f_x^D(k\Delta t)]^2 + [f_y^D(k\Delta t)]^2} \right]_T \tag{A.1b}$$

where $\boldsymbol{\theta}_D$ is a vector of the parameters of device D, and the device force predictions $\hat{f}_x^D(t;\boldsymbol{\theta}_D)$ and $\hat{f}_y^D(t;\boldsymbol{\theta}_D)$ are computed from the device model in (9) or (10)–(11) driven by the drifts and corresponding drift velocities across device D measured during test T. The steps of the first level are:

1a. **RBs**: For a candidate RBi preyield stiffness $k^{\text{RB}i} = k_{xx}^{\text{RB}i} = k_{yy}^{\text{RB}i}$, taken from a set of $n_{\text{RB}i}$ (which is 7 herein) candidate values evenly spanning the range [1025,1175] kN/m (approximately the LB and UB of RB stiffnesses in Table 6), determine the postyield stiffness $\bar{k}^{\text{RB}i}$ and

yield displacement $\bar{u}^{\mathrm{RB}i}$ that minimize $E_{\mathrm{RB}i}([k^{\mathrm{RB}i} \;\; \bar{k}^{\mathrm{RB}i} \;\; \bar{u}^{\mathrm{RB}i}]^{\mathrm{T}})$ using (A.1) for RBi.

1b. **ESB1**: For a pair of lower bounds on ESB1 damping coefficients c_{xx}^{ESB1} and c_{yy}^{ESB1} — each taken from a set of n_{ESB1} (which is 6 herein) bounds evenly spanning $[0, 50]$ Mg/s, thus forming a grid of n_{ESB1}^2 pairs — find the ESB1 parameter vector $\boldsymbol{\theta}_{\mathrm{ESB1}} = [c_{xx}^{\mathrm{ESB1}} \;\; c_{yy}^{\mathrm{ESB1}} \;\; \beta^{\mathrm{ESB1}} \;\; \gamma^{\mathrm{ESB1}}]^{\mathrm{T}}$ that minimize $E_{\mathrm{ESB1}}(\boldsymbol{\theta}_{\mathrm{ESB1}})$. (Note: $A^{\mathrm{ESB}i} \equiv \beta^{\mathrm{ESB}i} + \gamma^{\mathrm{ESB}i}$.)

1c. **ESB2**: Identical to ESB1 except the damping coefficient lower bounds span $[0, 30]$ Mg/s (and n_{ESB2} is taken to be 4 herein).

1d. **SDPs**: For a candidate lower bound on c_{xx}^{SDP} and c_{yy}^{SDP} (the same lower bound for both directions and both SDPs) — taken from a set of n_{SDP} (which is 11 herein) SDP damping coefficient lower bounds evenly spanning $[0, 100]$ Mg/s — determine the set of SDP parameters $\boldsymbol{\theta}_{\mathrm{SDP}} = [k_{xx}^{\mathrm{SDP}} \;\; k_{yy}^{\mathrm{SDP}} \;\; c_{xx}^{\mathrm{SDP}} \;\; c_{yy}^{\mathrm{SDP}} \;\; \alpha^{\mathrm{SDP}} \;\; \beta^{\mathrm{SDP}} \;\; \gamma^{\mathrm{SDP}}]^{\mathrm{T}}$ that minimizes the sum $E_{\mathrm{SDP}}(\boldsymbol{\theta}_{\mathrm{SDP}}) = E_{\mathrm{SDP1}}(\boldsymbol{\theta}_{\mathrm{SDP}}) + E_{\mathrm{SDP2}}(\boldsymbol{\theta}_{\mathrm{SDP}})$.

Lower bounds on the ESB and SDP damping coefficients are needed to ensure that the effective modal damping ratios identified from the predicted partially nonlinear FEM responses to the low-level random excitations rise to the level reported in Table 2; the upper end of the ranges for the sets of lower bounds are chosen to limit the increases in corresponding optimal device force cost metric — *i.e.*, $E_{\mathrm{ESB1}}(\boldsymbol{\theta}_{\mathrm{ESB1}})$, $E_{\mathrm{ESB2}}(\boldsymbol{\theta}_{\mathrm{ESB2}})$ or $E_{\mathrm{SDP}}(\boldsymbol{\theta}_{\mathrm{SDP}})$ — to no more than 15% above the optimal metric when the lower bound is zero.

The second level of the optimization strategy then chooses from among

the first level's set of $n_{\text{combos}} = n_{\text{RB1}} \cdot n_{\text{RB2}} \cdot n_{\text{ESB1}}^2 \cdot n_{\text{ESB2}}^2 \cdot n_{\text{SDP}}$ combinations of RB1, RB2, ESB1, ESB2 and SDP optimal parameters, which may be denoted $\boldsymbol{\theta}_1, \ldots, \boldsymbol{\theta}_{n_{\text{combos}}}$. For each of the n_{combos} combinations, the partially nonlinear FEM time-history responses to low-level random excitation in Test 010 are computed; the relative errors in the predicted RMS of each of the twelve (six devices, each with two directions) isolation-layer device horizontal force time histories are computed. The second level then chooses the combination of parameters that provides the smallest of the largest device force errors. In other words, choose the combination

$$\arg \min_{k \in \{1,2,\ldots,n_{\text{combos}}\}} \max_{\substack{i \in \{1,2\} \\ D \in \{\text{RB,ESB,SDP}\}}} \max_{w \in \{f_x^{Di}, f_y^{Di}\}} Err_w^{\text{RMS}}(\boldsymbol{\theta}_k) \tag{A.2}$$

The resulting combination of optimal parameters is then listed in Table 10; this optimal combination indeed results in relative errors in Test 010 RMS forces only marginally larger than those reported in Table 9 for the purely linear FEM (to force them the same would mean less faithful reproduction of the earthquake responses such as in Test 016).

Note that, in some of the first level's combinations, some optimal damping coefficients do converge to their corresponding lower bounds; indeed, the optimal parameters chosen in the second level is such a case, resulting in the damping coefficients for ESB2 and the SDPs to be at their corresponding discrete lower bound values, as shown in Table 10.

Appendix B. Data and Code Availability

To facilitate future simulation studies on this full-scale based-isolated building, the following data and MATLAB® codes will be made available in the DesignSafe-CI "Data Depot": (a) table-center acceleration records computed from the shake table acceleration measurements during random excitation and earthquake ground motion tests; (b) system matrices **M** and **K** of the unupdated and updated superstructure linear FEMs; (c) codes for finding the node closest to any given 3D coordinates; (d) codes for time-history analyses using different isolation-layer device models; and (e) codes to simulate the response of the partially nonlinear FEM.

References

Allemang, R.J., Brown, L.D., 1982. A correlation coefficient for modal vector analysis, in: Proceedings of the 1st International Modal Analysis Conference, pp. 110–116.

Avitabile, P., O'Callahan, J.C., 1988. Model correlation and orthogonality criteria, in: Proceedings of the 6th International Modal Analysis Conference, pp. 1039–1047.

Bakir, P.G., Reynders, E., De Roeck, G., 2007. Sensitivity-based finite element model updating using constrained optimization with a trust region algorithm. Journal of Sound and Vibration 305, 211–225.

Bakir, P.G., Reynders, E., De Roeck, G., 2008. An improved finite element model updating method by the global optimization technique 'Coupled Local Minimizers'. Computers & Structures 86, 1339–1352.

Beck, J.L., Au, S.K., Vanik, M.W., 2001. Monitoring structural health using a probabilistic measure. Computer-Aided Civil and Infrastructure Engineering 16, 1–11.

Beck, J.L., Katafygiotis, L.S., 1998a. Updating models and their uncertainties. I: Bayesian statistical framework. Journal of Engineering Mechanics 124, 455–461.

Beck, J.L., Katafygiotis, L.S., 1998b. Updating models and their uncertainties. II: Model identifiability. Journal of Engineering Mechanics 124, 463–467.

Beck, J.V., Arnold, K.J., 1977. Parameter estimation in engineering and science. John Wiley & Sons.

Brewick, P.T., Johnson, E.A., Sato, E., Sasaki, T., 2018. Constructing and evaluating generalized models for a base-isolated structure. Structural Control and Health Monitoring 25, e2243.

Brewick, P.T., Johnson, E.A., Sato, E., Sasaki, T., 2020. Modeling the dynamic behavior of isolation devices in a hybrid base-isolation layer of a full-scale building. Journal of Engineering Mechanics 146, 04020127.

Bugeat, L.P., Lallement, G., 1976. Methods of matching calculated and identified eigensolutions. Storjnicky Casopis 32, 162–167.

Constantinou, M.C., Mokha, A.S., Reinhorn, A.M., 1990. Teflon bearings in base isolation. II: modeling. ASCE Journal of Structural Engineering 116, 455–474.

Cornwell, P., Doebling, S.W., Farrar, C.R., 1999. Application of the strain energy damage detection method to plate-like structures. Journal of Sound and Vibration 224, 359–374.

Everitt, B.S., Landau, S., Leese, M., Stahl, D., 2001. Cluster Analysis. John Wiley & Sons, Ltd, London.

Friswell, M., Mottershead, J.E., 2013. Finite element model updating in structural dynamics. volume 38. Springer Science & Business Media.

Hu, S.L.J., Li, H., Wang, S., 2007. Cross-model cross-mode method for model updating. Mechanical Systems and Signal Processing 21, 1690–1703.

Hu, S.L.J., Wang, S., Li, H., 2006. Cross-modal strain energy method for estimating damage severity. Journal of Engineering Mechanics 132, 429–437.

Ibrahim, S.R., 1993. Correlation and updating methods: finite element dynamic model and vibration test data, in: International Conference on Structural Dynamics Modelling, Test, Analysis and Correlation, pp. 323–347.

Ierimonti, L., Venanzi, I., Cavalagli, N., Comodini, F., Ubertini, F., 2020. An innovative continuous Bayesian model updating method for base-isolated RC buildings using vibration monitoring data. Mechanical Systems and Signal Processing 139.

Imregun, M., Visser, W.J., Ewins, D.J., 1995. Finite element model updating using frequency response function data: I. theory and initial investigation. Mechanical Systems and Signal Processing 9, 187–202.

Jang, J., Smyth, A.W., 2017a. Bayesian model updating of a full-scale finite elementmodel with sensitivity-based clustering. Struct Control and Health Monitoring 24, e2004.

Jang, J., Smyth, A.W., 2017b. Model updating of a full-scale FE model with nonlinear constraint equations and sensitivity-based cluster analysis for updating parameters. Mechanical Systems and Signal Processing 83, 337–355.

Juang, J.N., Pappa, R.S., 1985. An eigensystem realization algorithm for modal parameter identification and model reduction. Journal of guidance, control, and dynamics 8, 620–627.

Li, Y., Wang, S., Xia, Z., An, W., 2020. An iterative total least squares-based estimation method for structural damage identification of 3D frame structures. Structural Control and Health Monitoring 27, e2499.

Lieven, N.A.J., Ewins, D.J., 1988. Spatial correlation of mode shapes, the coordinate modal assurance criterion (COMAC), in: Proceedings of the 6th International Modal Analysis Conference, pp. 690–695.

Lin, R.M., 2011. Identification of modal parameters of unmeasured modes using multiple FRF modal analysis method. Mechanical Systems and Signal Processing 25, 151–162.

Lin, R.M., Ewins, D.J., 1994. Analytical model improvement using frequency response functions. Mechanical Systems and Signal Processing 8, 437–458.

Lin, R.M., Zhu, J., 2006. Model updating of damped structures using FRF data. Mechanical Systems and Signal Processing 20, 2200–2218.

Moaveni, B., Conte, J.P., Hemez, F.M., 2009. Uncertainty and sensitivity analysis of damage identification results obtained using finite element model updating. Computer-Aided Civil and Infrastructure Engineering 24, 320–334.

Mokha, A.S., Constantinou, M.C., Reinhorn, A.M., 1993. Verification of friction model of Teflon bearings under triaxial load. ASCE Journal of Structural Engineering 119, 240–261.

Nakashima, M., Nagae, T., Enokida, R., Kajiwara, K., 2018. Experiences, accomplishments, lessons, and challenges of E-defense—Tests using world's largest shaking table. Japan Architectural Review .

O'Callahan, J.C., 1995. Development of a general pseudo orthogonality correlation procedure, in: Proceedings of the 13th International Modal Analysis Conference, pp. 1013–1021.

Ogawa, N., Ohtani, K., Katayama, T., Shibata, H., 2001. Construction of a three-dimensional, large-scale shaking table and development of core technology. Philosophical Transactions of the Royal Society of London. Series A: Mathematical, Physical and Engineering Sciences 359, 1725–1751.

Park, Y.J., Wen, Y.K., Ang, A.H.S., 1986. Random vibration of hysteretic systems under bi-directional ground motions. Earthquake Engineering and Structural Dynamics 14, 543–557.

Peeters, B., 2000. System identification and damage detection in civil engineering. Ph.D. thesis. Katholieke Universiteit te Leuven.

Sato, E., Sasaki, T., Fukuyama, K., Tahara, K., Kajiwara, K., 2013. Development of innovative base isolation system based on E-Defense full-scale shake table experiments part I: Outline of project research, in: AIJ Annual Meeting. Hokkaido, Japan, pp. 751–752. (in Japanese).

Shadan, F., Khoshnoudian, F., Esfandiari, A., 2016. A frequency response-based structural damage identification using model updating method. Structural Control and Health Monitoring 23, 286–302.

Shahverdi, H., Mares, C., Wang, W., Mottershead, J.E., 2009. Clustering of

parameter sensitivities: examples from a helicopter airframe model updating exercise. Shock and Vibration 16, 75–87.

Shi, Z., Law, S.S., Zhang, L.M., 1998. Structural damage localization from modal strain energy change. Journal of Sound and Vibration 218, 825–844.

Song, W., Dyke, S.J., Harmon, T.G., 2012. Application of nonlinear model updating for a reinforced concrete shear wall. Journal of Engineering Mechanics 139, 635–649.

Song, W., Dyke, S.J., Harmon, T.G., So, M., 2009a. Nonlinear model updating in concrete structures based on ambient response data, in: Proceedings of the 27th International Modal Analysis Conference, pp. 679–690.

Song, W., Dyke, S.J., Yun, G., Harmon, T.G., 2009b. Improved damage localization and quantification using subset selection. Journal of Engineering Mechanics 135, 548–560.

Stubbs, N., Kim, J.T., Farrar, C.R., 1995. Field verification of a nondestructive damage localization and severity estimation algorithm, in: Proceedings of the 13th International Modal Analysis Conference, 13–16 February 1995, Nashville, TN, Society for Experimental Mechanics, Inc., Bethel, CT. pp. 210–218.

Ueda, T. (Ed.), 2007. Standard specifications for concrete structures – 2007 'Design'. JSCE Guidelines for Concrete, JSCE, No. 15.

Vacher, P., Jacquier, B., Bucharles, A., 2010. Extensions of the MAC criterion to complex modes, in: Proceedings of the International Conference on Noise and Vibration Engineering, pp. 2713–2726.

Van Overschee, P., De Moor, B., 1994. N4SID: Subspace algorithms for the identification of combined deterministic-stochastic systems. Automatica 30, 75–93.

Vanik, M.W., Beck, J.L., Au, S., 2000. Bayesian probabilistic approach to structural health monitoring. Journal of Engineering Mechanics 126, 738–745.

Wang, S., Li, Y., Li, H., 2015. Structural model updating of an offshore platform using the cross model cross mode method: An experimental study. Ocean Engineering 97, 57–64.

Wang, S., Xu, M., 2019. Modal strain energy-based structural damage identification: a review and comparative study. Structural Engineering International 29, 234–248.

Wen, Y.K., 1980. Equivalent linearization for hysteretic systems under random excitation. ASME Journal of Applied Mechanics 47, 150–154.

Yang, X., Ouyang, H., Guo, X., Cao, S., 2020. Modal strain energy-based model updating method for damage identification on beam-like structures. Journal of Structural Engineering 146, 04020246.

Yu, T., 2022. Novel Multi-Stage and CTLS-Based Model Updating Methods and Real-Time Neural Network–Based Semiactive Model Predictive Control Algorithms. Ph.D. thesis. University of Southern California. Los Angeles, CA.

Yu, T., Johnson, E.A., 2022a. CTLS-based CMCM model updating method. Under preparation.

Yu, T., Johnson, E.A., 2022b. Neural network accelerated semi-active model predictive control. Under preparation.